Numerical study of the dynamic responses of precast epoxy asphalt cured track (PEACT) transition zone

Wu, You; Shi, Chenguang; Yu, Yunhong; Fan, Yulou; Yang, Jun

DOI
10.1016/j.rineng.2025.108453

Publication date
2025

Document Version
Final published version

Published in
Results in Engineering

Citation (APA)
Wu, Y., Shi, C., Yu, Y., Fan, Y., & Yang, J. (2025). Numerical study of the dynamic responses of precast epoxy asphalt cured track (PEACT) transition zone. *Results in Engineering*, *28*, Article 108453. https://doi.org/10.1016/j.rineng.2025.108453

Results in Engineering 28 (2025) 108453

Contents lists available at ScienceDirect

Results in Engineering

journal homepage: www.sciencedirect.com/journal/results-in-engineering

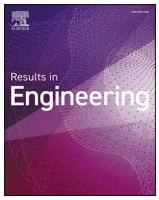

Numerical study of the dynamic responses of precast epoxy asphalt cured track (PEACT) transition zone

You Wu [a,*], Chenguang Shi [b,*], Yunhong Yu [c], Yulou Fan [c], Jun Yang [c,*]

[a] Section of Railway Engineering, Delft University of Technology, Stevinweg 1 2628 CN, Delft, the Netherlands
[b] National & Local Joint Engineering Research Center of Transportation Civil Engineering Materials, Chongqing Jiaotong University, Chongqing 400074, China
[c] School of Transportation, Southeast University, #2 Southeast University Road, Nanjing 211189, China

ARTICLE INFO

Keywords:
High-speed railway
Dynamic responses
Transition zone
Pre-cast asphalt track
Numerical implementation

ABSTRACT

The rapid advancement of high-speed railway (HSR) has imposed significantly higher demands on rail tracks' performance and vibration mitigation capabilities, necessitating the design of track systems that can withstand extreme operational conditions while ensuring passenger comfort. Precast epoxy asphalt-cured track (PEACT) has emerged as a promising solution, offering superior mechanical properties and environmental adaptability. In this study, a full-scale finite-element model of PEACT is established and validated. Four dry-mixed rubberised epoxy asphalt mixtures (DREAMs) are incorporated, with their material parameters (e.g., modulus, density, damping) explicitly defined. Several modelling enhancements are implemented beyond conventional response analysis, including: (i) DREAM-grade-specific Rayleigh damping calibration derived from modal analysis, (ii) a stability-first boundary–mesh prescription. These strategies improve modelling fidelity for non-uniform transition zones. The results show that PEACT dynamic responses remain within acceptable ranges, and that DREAMs provide substantial vibration attenuation, contributing an additional ~40% reduction on top of the fastener system. From a design perspective, these findings provide practical evidence that graded DREAM layouts can effectively control vertical surface displacement to below 0.5 mm under 350 km/h loading, facilitating smoother stiffness transitions, reduced maintenance demand, and more reliable HSR operation.

1. Introduction

As a high-efficiency, safe, and convenient transport method that also reduces carbon emissions, high-speed railway (HSR) technology has seen significant progress over the past several decades. Taking China as an example, its total miles of HSR had reached 45,000 km by 2023 and is expected to extend to 70,000 km by the year 2035 [1]. Along with the rapid growth in mileage, the coverage area of HSR has also become increasingly extensive, posing a more significant challenge for HSR tracks to be suitable for different regions while maintaining passenger comfort.

Facing such strict demands, the traditional ballasted or ballastless track shows its disadvantages in further popularization. On the one hand, the unbounded ballast in the ballasted track is easily displaced and broken under repeated train loadings, resulting in permanent vertical track deformation and geometric degradation. To overcome this issue, regular and frequent maintenance is required to maintain the serviceability of the track structure [2,3], which involves a significant investment [4]. Additionally, the unbounded ballast poses a potential threat to passing trains, such as the potential for flying ballast [5–7]. On the other hand, the intrinsic disadvantages of a ballastless track, such as sizeable wheel-rail contact forces and low flexibility, also limit its comfortableness and long-term service quality [8–10].

In response to these problems, the cured track, e.g., bitumen-stabilized track [8,9], polyurethane-reinforced track [10,11], and epoxy asphalt-cured track [11,12], has been proposed, which bounds the ballast with viscoelastic materials. Typically, the polyurethane track has been successfully applied to the Yinchuan-Xi'an high-speed line in China, maintaining excellent service qualities [13]. However, there are still limitations regarding existing forms of cured track. For example, bitumen-stabilized asphalt tracks, especially those stabilized with emulsified asphalt, can be challenging to maintain long-term stability due to their low moisture resistance and strength [10,14,15]. Moreover, the wide application of polyurethane tracks is also limited due to the high construction costs and the strict demand for construction sites [13,16,17].

* Corresponding authors.
E-mail addresses: You.Wu@tudelft.nl (Y. Wu), chenguangshi@cqjtu.edu.cn (C. Shi), yangjun@seu.edu.cn (J. Yang).

https://doi.org/10.1016/j.rineng.2025.108453
Received 25 September 2025; Received in revised form 25 November 2025; Accepted 26 November 2025
Available online 27 November 2025

To overcome these difficulties, epoxy asphalt mixture (EAM), which has been widely used in pavement engineering, bridge deck paving, and airport runways, draws attention because of its excellent mechanical characteristics and long-term stability [18–21]. In railway engineering, previous research proposed the form of applying EAM, i.e., the precast epoxy asphalt cured track (PEACT) [12,22]. Referenced from the existing polyurethane track, the under-rail double block precast structure was applied in PEACT [17]. Firstly, specially designed EAM blocks can be prefabricated in plants or factories, as shown in Fig. 1(a). Then, these blocks are transmitted to the construction site and composed into basic PEACT units using epoxy asphalt mortar [23,24], as shown in Fig. 1(b). The left image shows the bonding between the cement concrete sleeper and DREAM blocks, and the right image shows the specimen of the basic PEACT unit. Subsequently, these blocks will be arranged sequentially. A detailed arrangement scheme is presented in Ref [11], and the schematic of the PEACT overview is shown in Fig. 1(c).

Previous studies have extensively examined the design method of the core material in PEACT, namely the dry-mixed epoxy asphalt mixture (DREAM) [11,22,24]. The applicability of DREAM in normal track sections [12,24] and its key mechanical properties [23,25–27] have been investigated in detail. However, to further advance the practical implementation of PEACT, it is essential to clarify the fundamental material requirements, assess their performance in specific structural zones such as the transition zone, and examine their mechanical behavior under these conditions. Existing research primarily focuses on comparing PEACT and polyurethane tracks in terms of overall mechanical responses, but lacks systematic analyses of the material requirements and detailed mechanical response characteristics of PEACT in transition zones [11].

Regarding the analysis of dynamic responses in transition zones, the finite element method (FEM) has become increasingly reliable and widely adopted with the advancement of computational technology. For example, Wang and Markine [28,29] established a comprehensive train-track coupling dynamic model of the embankment-bridge transition zone, in which the dynamic response and influence of settlement of the transition zone were investigated in detail. Jing et al [30] verified

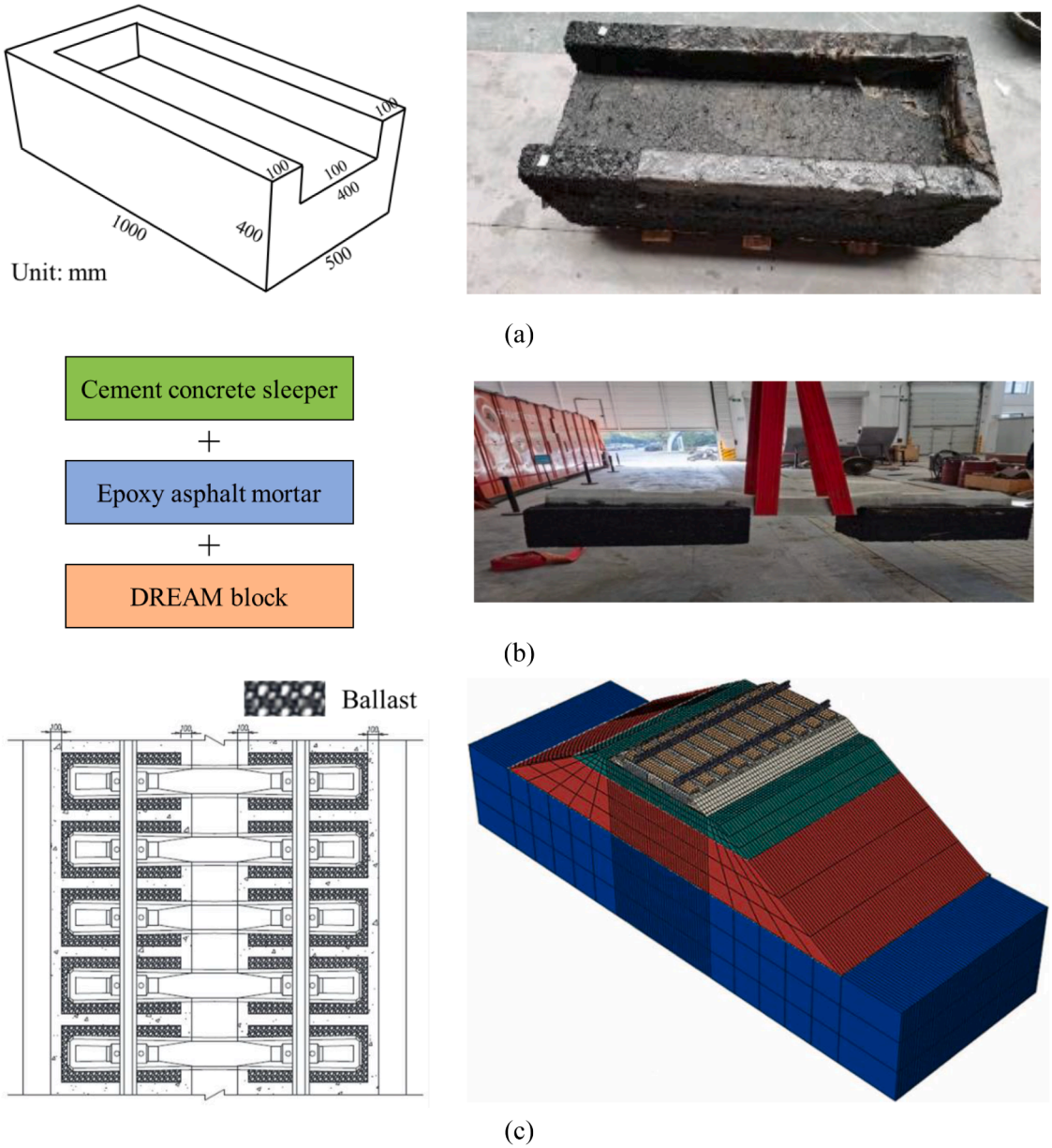

Fig. 1. Schematic of (a) EAM blocks (left: block size, right: block specimen), (b) basic unit of PEACT (left: bonding between sleeper and block, right: basic unit of PEACT), and (c) overview of whole PEACT structure (left: top view, right: FE model of regular track section).

the feasibility of using furnace slag to achieve smoother variations in dynamic responses within the transition zone through FE modeling, further demonstrating the rationality of FEM in such studies.

However, in the context of PEACT, although several FEM-based investigations have been conducted for both normal track sections [12,22] and transition zones [11], existing research still exhibits methodological limitations. In particular, key modeling parameters such as boundary conditions [31], time step [32], mesh size [33], et al., have been shown to significantly affect computational accuracy, yet these factors are not thoroughly addressed in prior PEACT studies [11,12]. Therefore, to further promote the application of PEACT and strengthen its theoretical foundation, a more comprehensive investigation into the material requirements and dynamic characteristics of transition zones is still required.

Building upon previous studies [12,13,22–24,27], this study first refines the finite element (FE) model used to characterize the dynamic responses of typical track–bridge transition zones, as described in Section 2. The modified model can also be extended to analyze the dynamic behavior of other types of transition zones. Subsequently, a representative arrangement of designed DREAMs within the transition zone is employed to demonstrate the feasibility and advantages of incorporating DREAMs into the track structure, as discussed in Section 3. Section 4 proposed some possible future improvements of the established model and design scheme of PEACT. Finally, the key results and conclusions of this study are summarized in Section 5.

2. Modeling the transition zone

2.1. Model settings

This study establishes two forms of track models to investigate different aspects of dynamic responses. The first model (M-I) is a full-scale average track model consisting of 5 sleepers, as shown in Fig. 2 (a), which is used to examine the influence of crumb rubber (CR) content on the dynamic response. The second model (M-II) is a full-scale track–bridge transition zone model with a total length of 90 m, comprising a 30 m bridge section and two 30 m transition zones on either side, as shown in Fig. 2(b). This model is used to investigate the influence of train running direction on dynamic responses and to characterize the dynamic behavior of the transition zone.

The basic configuration of M-II follows Ref [11]. This paper only introduces the differences between M-I and M-II, as well as the modifications of M-II. To eliminate the effects of FE model boundaries and the coupling interactions between adjacent track sections with different materials, M-I adopts a simplified partial model of the track structure consisting of five sleepers and a single wheel model. This approach has been validated as reasonable in Refs [34,35] and its equations can be found in Appendix A.1 and A.2. Specifically, the M-I is 6 m in height, 17.8 m in width, and 3 m in length, which can be seen as a reasonable size for a length-reduced FE model of track structure [34]. The viscous boundary, whose reasonability is illustrated in Section 2.2.1, is applied to mitigate the influence of the boundary effect.

Several modifications were made to M-II compared with the model presented in Ref [11]. Firstly, a groove layer is added between the DREAM blocks and the surface layer to ensure that all blocks are leveled, in accordance with engineering practice. Then, the Timoshenko beam element is employed to simulate the rail and sleeper, thereby improving efficiency [36,37]. Besides, penalty contact is employed to simulate contact among different track structures, the detailed theories of which can be found in Appendix A.3. Other important settings are consistent with Ref [11]. The spring-damping elements are used to simulate the fasteners between the rail and the sleeper. The damping and stiffness of the fasteners are 50 kN·s^{-1} [29] and 50 kN·mm^{-1} [38], respectively. Apart from these parts, all other parts of the track structure are modeled with solid element C3D8R. The arrangement method of DREAM blocks remains the same as Ref [11], which consists of 10 EA-6 CR blocks, 20 EA-4 CR blocks, 10 EA-2 CR blocks, and 10 EA-0 CR blocks (10–20–10–10) from the trackside to the bridge side. Here, EA-x CR means epoxy asphalt mixture containing x % CR (corresponding to different kinds of DREAMs), and the gradation and mechanical properties can be found in Ref [39]. Detailed equations for the dynamic model of the track structure are presented in Appendix A.1, and the corresponding element matrix is provided in Appendix B.

2.2. Model updating

In addition to the modifications to the basic model configuration, this section further refines the model accuracy through a detailed comparison of different modeling settings and key analytical parameters, including modal analysis, selection of boundary conditions, and determination of the optimal mesh size.

2.2.1. Modal analysis

The damping coefficients of the DREAMs need to be determined first. Based on the Rayleigh damping theory and the dynamic analysis theory [40], the relationship between the damping ratio ξ and Rayleigh damping coefficients α, β can be written as Eq. (1):

$$\xi = \frac{\alpha}{2\omega} + \frac{\beta\omega}{2} \tag{1}$$

where ω is the self-oscillation frequency of the structure. According to Eq. (1), once the first two order self-oscillation frequencies ω_1 and ω_2 were obtained, the α, β can be calculated as follows:

$$\begin{cases} \alpha = \dfrac{2\xi\omega_1\omega_2}{\omega_1 + \omega_2} \\ \beta = \dfrac{2\xi}{\omega_1 + \omega_2} \end{cases} \tag{2}$$

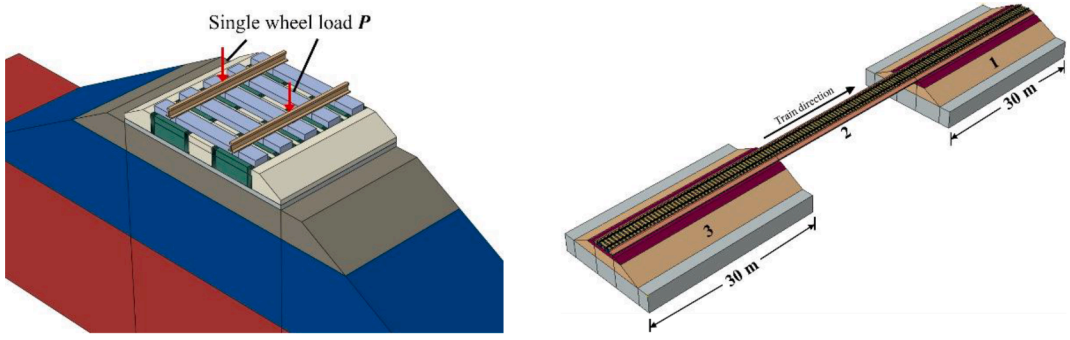

Fig. 2. Schematic of (a) full-scale normal track model with a length of 5 sleepers (M-I), and (b) full-scale track-bridge transition zone model (M-II).

Based on this theory, a modal analysis of the structure is conducted before proceeding with the dynamic response analysis. The damping ratios of four kinds of DREAMs are obtained from Ref [39], and the values are 0.2542 for EA-6 CR, 0.2353 for EA-4 CR, 0.1792 for EA-2 CR, and 0.1658 for EA-0 CR. Fig. 3 shows the results of the modal analysis for the first 10-order self-oscillation frequencies.

It should be noted that, in the modal analysis, only the viscoelastic parameters differ among the materials, while the elastic modulus, material density, and boundary conditions of the structure remain identical. Therefore, the structure is expected to exhibit the same natural frequencies, with only the damping characteristics being affected. Consequently, only one legend EA is used to present all four kinds of DREAMs in Fig. 3. The Rayleigh damping coefficients α and β obtained from DREAMs, calculated using Eq. (2), are listed in Table 1. These coefficients are used as key material parameters for calculating structural accelerations subsequently.

Table 1
Self-oscillation frequencies of the structure and Rayleigh damping coefficients of DREAMs.

Material	EA-0 CR	EA-2 CR	EA-4 CR	EA-6 CR
ξ	0.1658	0.1792	0.2353	0.2542
ω_1	0.57179	0.57179	0.57179	0.57179
ω_2	0.5903	0.5903	0.5903	0.5903
α	0.09631	0.1041	0.1367	0.1477
β	0.2853	0.3084	0.4050	0.4375

2.2.2. *Boundary conditions*

Two types of boundaries, the infinite boundary and the viscous boundary, are separately applied to Model II (M-II) to determine the most appropriate setting for subsequent analyses. Detailed theories and setting methods can be found in Ref [41] and Ref [42]. As illustrated in Fig. 4, the new boundaries are positioned along the normal embankment sides in the longitudinal direction of the surface, bottom, and base layers, as well as along the lateral sides of the base layer. Fixed boundaries are assigned to the bottom of the base layer. On the face adjacent to the bridge, fixed boundaries are applied to the bottom edges of the surface, bottom, and base layers to simulate potential reinforcement of the embankment in engineering practice, thereby preventing excessive displacement near the bridge. The remaining portions of this face and sloped surfaces are left free.

Taking the vertical displacement at the top of the surface layer and the vertical displacement at the top of asphalt blocks as examples, both of which are sensitive to boundary conditions [31], Fig. 5(a) and Fig. 5 (b) compare the effectiveness of applying different boundaries. As shown in fig. 2(b), the model in this study is symmetric. Therefore, the only difference between track sections 1 and 3 lies in the direction of train movement, which exerts a limited influence on the overall dynamic response. Accordingly, the dynamic response of the middle region of track section 3 during the first 0.6 s is analyzed to evaluate the effectiveness of various boundary settings.

As illustrated in Fig. 5, the dynamic response of the entire model exhibits intense oscillatory behavior when the normal boundary is

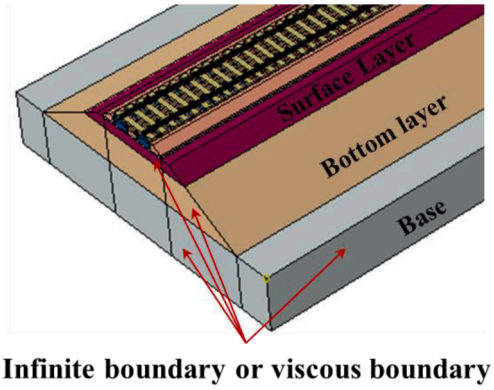

Fig. 4. Locations of infinite elements and viscous boundaries.

employed. This approach only captures the passage of train loads through specific cross-sections, but it needs to be more reliable in reflecting the temporal characteristics of dynamic responses. In contrast, the infinite and viscous boundaries significantly mitigate the influence of boundary effects on computational accuracy. The results indicate that these two methods effectively suppress the reflected waves that distort the calculated dynamic responses, with only minor oscillations observed after the load passes—oscillations that do not affect the accuracy of the results. Among them, the viscous boundary provides greater stability than the infinite boundary. During the initial phase of load application, the viscous boundary exhibits almost no fluctuations caused by reflected waves, whereas the infinite boundary still shows noticeable oscillations, as illustrated in Fig. 5(b). Nevertheless, it should be emphasized that neither boundary type can completely eliminate the influence of reflected waves. The following section further investigates these effects using results obtained with the viscous boundary.

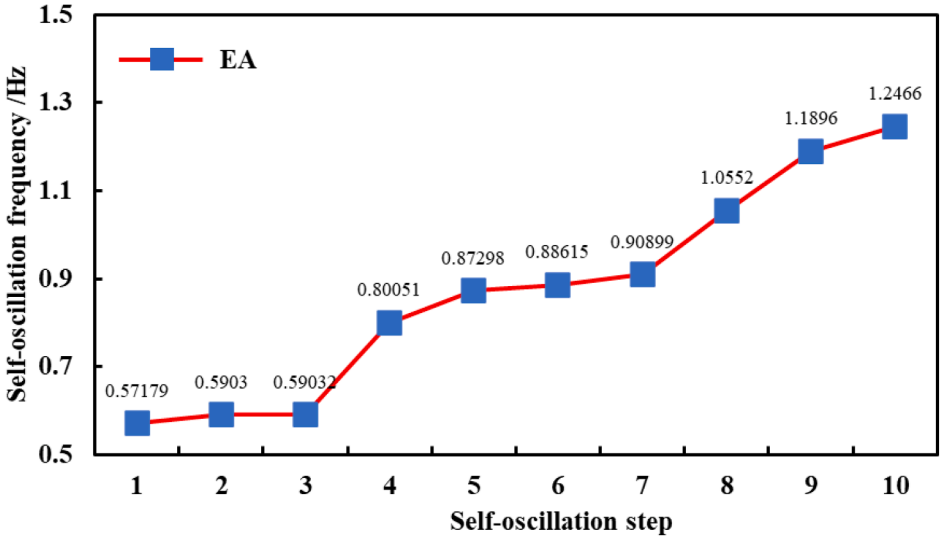

Fig. 3. The first ten orders of self-oscillation frequencies for DREAMs.

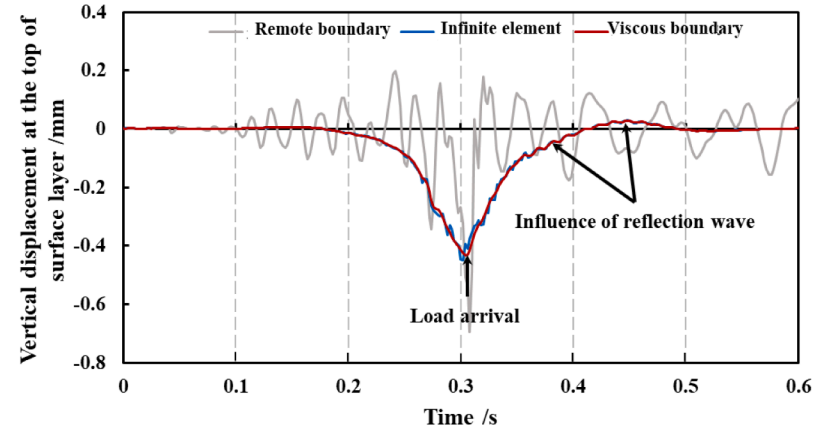

(a)

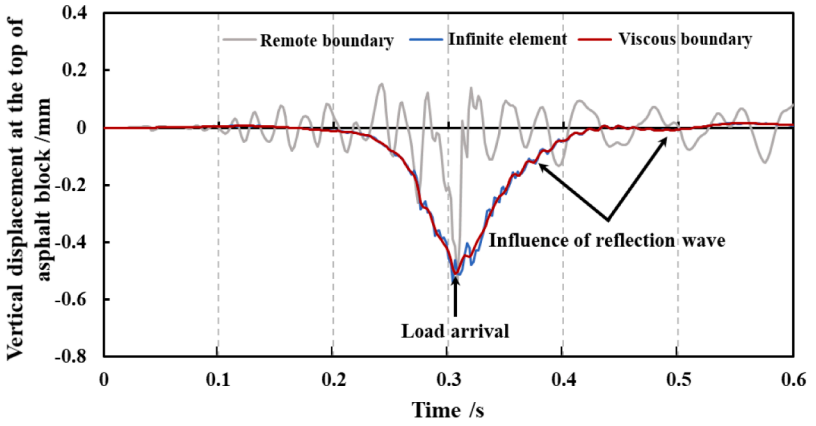

(b)

Fig. 5. Comparison of three kinds of boundary conditions, taking (a) vertical displacement at the top of the surface layer, and (b) vertical displacement at the top of the asphalt block, as examples.

As shown in Fig. 5, the dynamic response peaks at approximately 0.3 s, corresponding to the train load crossing the midpoint of track section 3. Before this point, the dynamic response gradually increases from near zero. The deformation at the selected location decreases once the train load moves away from this cross-section. Once the train load moves away from the cross-section, the deformation decreases but not monotonically—oscillations are observed, particularly between 0.4 and 0.5 s. These fluctuations are attributable to boundary-reflected waves returning to the observation section. According to Shih et al [31], when the lateral width of the track bed model is relatively small ($\leq$20 m), and the train speed is relatively high ($\geq$60 m/s), reflected waves become prominent laterally and may affect computational accuracy. In this study, infinite and viscous boundaries were applied along the longitudinal direction of the base layer; however, the lateral elimination of reflected waves in other trackbed components remained infeasible, making some boundary effects inevitable. Considering both computational efficiency and numerical stability, the viscous boundary condition is adopted for subsequent analyses in this study.

2.2.3. *Mesh sensitivity*

Another key factor influencing computational accuracy in finite element (FE) analysis is mesh size, particularly in large-scale models where a balance between accuracy and efficiency must be maintained. In this study, specific components of the track bed model, including the base layer, bottom layer, and ballast, are not the focus of analysis. Since these components are located near the model boundaries, they exert minimal influence on the results in critical regions. To improve computational efficiency, the mesh sizes of these components are fixed during the mesh sensitivity analysis and are not further refined.

For the primary components of interest, including the rail, sleeper, asphalt blocks, cement concrete pads, and surface layer, a mesh sensitivity study is conducted with element sizes of 0.6, 0.5, 0.4, 0.3, 0.2, 0.1, and 0.05 m. The results, represented by the maximum vertical stress at the bottom of the asphalt blocks and the maximum vertical acceleration at the top of the surface layer, are shown in Fig. 6(a) and Fig. 6(b). These Fig.s correspond to the cross-sections containing the 25th and 26th asphalt blocks in track sections 3 and 1, respectively. The results reveal that the dynamic responses exhibit a monotonic trend as the mesh becomes finer and eventually stabilize. When the mesh size decreases from 0.1 m to 0.05 m, the variation in dynamic response across all selected cross-sections is less than 6 %, indicating that the results have reached mesh convergence.

In terms of computational efficiency, the runtime for a mesh size of 0.05 m is approximately four times that of 0.1 m. Considering the extensive FE simulations required in this study, a mesh size of 0.1 m was ultimately adopted for the critical component, including rail, sleeper, asphalt blocks, cement concrete pads, and surface layer, to ensure both accuracy and efficiency.

2.3. *Model validation*

While validating the model, it is essential to note that the PEACT in

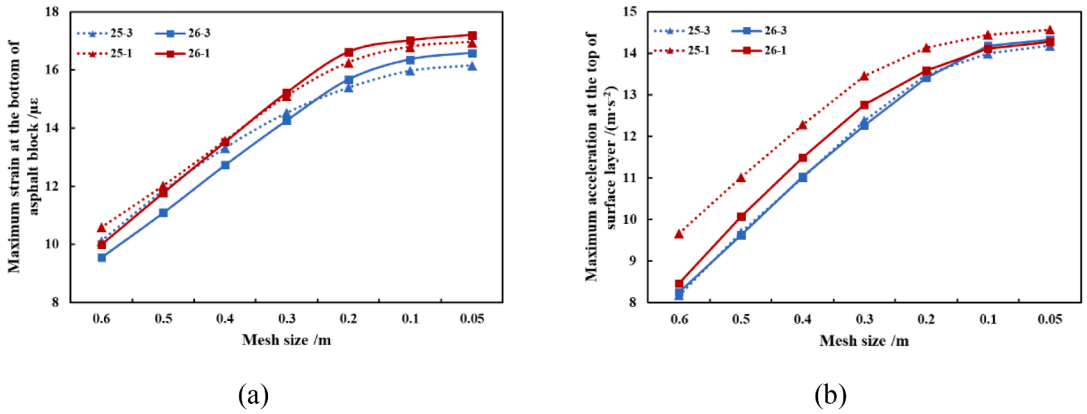

Fig. 6. Simulation results with different mesh sizes, taking (a) maximum strain at the bottom of the asphalt block, and (b) maximum acceleration at the top of the surface layer, as examples.

this study represents a novel form of track structure. Currently, the only comparable engineering application is the polyurethane trackbed used on the Yinchuan-Xi'an (Yin-Xi) High-Speed Railway [11]. Therefore, field data from the polyurethane-stabilized ballast bed of the Yin-Xi line were adopted for model validation. According to Ref [38], polyurethane exhibits viscoelastic behavior under dynamic loads, and its constitutive relationship can also be represented by a generalized Maxwell model, which is widely used to describe the behavior of epoxy asphalt materials [11,43]. In the FE model, the only difference between the polyurethane trackbed and the PEACT lies in their material parameters, whereas the structural configuration and constitutive formulations remain identical. The Prony series parameters for polyurethane are provided in Ref [38].

The static stiffness of the trackbed is first validated. Fig. 7(a) illustrates the static stiffness testing method, with the detailed implementation provided in Ref [11]. A comparison of the measured and simulated static stiffness results is presented in Fig. 7(b). The field-measured stiffness of the ballast bed structure was approximately 89.90 kN/mm, while the simulated stiffness was about 93.75 kN/mm, with a difference of less than 5 %. This close agreement demonstrates the reasonableness and reliability of the developed model.

Further validation is performed using dynamic responses. To align with field data, the vertical stress at the top of the surface layer and the vertical acceleration at the top of the surface layer were selected as comparison indicators. The numerical simulation results of the dynamic response are shown in Fig. 7(c) and Fig. 7(d). In these simulations, the material properties of all asphalt blocks are replaced with those of polyurethane, and the train speed is set to 300 km/h, corresponding to the actual conditions of the Yin-Xi HSR. The maximum vertical stress at

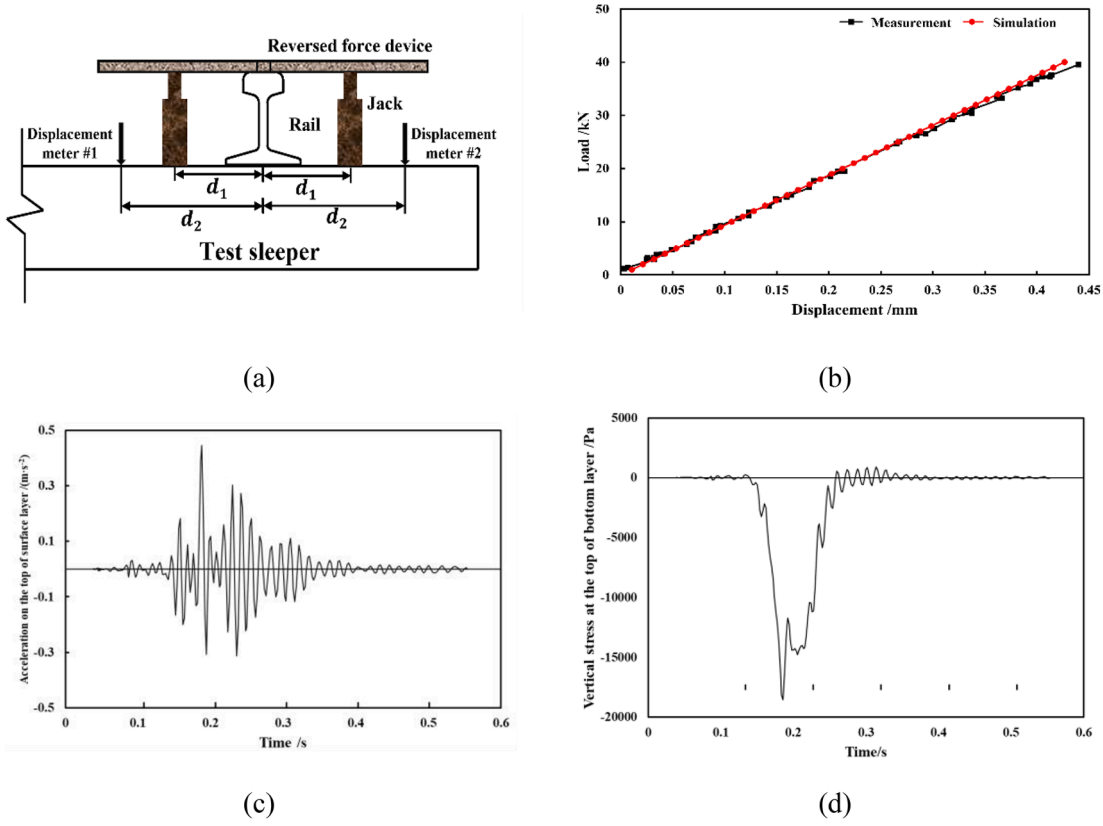

Fig. 7. (a) Schematic of static stiffness test, (b) comparison between simulated static stiffness and tested static stiffness, simulated time-history curve of (c) acceleration at the top of surface layer, and (d) vertical stress at the top of bottom layer.

the subgrade bottom and the maximum vertical acceleration at the top of the surface layer in the polyurethane trackbed model were 17.8 kPa and 0.45 m/s^2, respectively, only 4.49 % and 6.67 % higher than the measured values of 17 kPa and 0.42 m/s^2. These small deviations further confirm that the FE model developed in this study is accurate and reliable. Therefore, by substituting the polyurethane material parameters with those of the DREAMs, the validated model can be effectively applied to subsequent analyses.

2.4. Parameter selection

As a novel trackbed structure incorporating new materials, the PEACT still lacks systematic studies and standardized criteria for quantifying its structural dynamic responses. To address this gap, the present study aims to comprehensively characterize the mechanical response behavior of different components of the PEACT under high-speed train loading conditions. A total of 13 representative parameters associated with the mechanical performance of the PEACT were selected for analysis, as summarized in Table 2, with corresponding abbreviations.

These parameters are selected based on the following considerations. First, since the model in this study does not include the vehicle body, vehicle vibration-related parameters are excluded. Instead, attention is focused on the acceleration and displacement at the top of the rail, which directly reflect the dynamic performance transmitted to the track structure. Second, to assess the vibration attenuation capability of the DREAMs, the accelerations of five key components, i.e., the rail, sleeper, top and bottom of the asphalt blocks, and top of the surface layer, are included. Third, to ensure that the asphalt blocks can withstand a single train load without sustaining damage, the longitudinal and lateral strains at the bottom of the asphalt blocks are selected, following established practices in pavement engineering [44,45]. Finally, considering that Chinese standards [17,30] specify permissible displacement limits for various trackbed components, this study also considered the displacements at the top of the rail, the top of the asphalt block, and the top of the surface layer.

The locations of the data extraction points for these 13 parameters are shown in Fig. 8(a) and Fig. 8(b). Dynamic response values are collected at the cross-sections corresponding to each sleeper's center. Fig. 8(a) also shows the positions of the first three data collection cross-sections. The data from each cross-section are also used to assess the lateral distribution of the dynamic response. In the vertical direction, the dynamic response data are extracted from the top of the rail, the top of the sleeper, the top and bottom of the DREAM blocks, and the top of the surface layer at each cross-section. The average values at four nodes on the same plane are used as the structural dynamic response value for subsequent analyses.

Table 2
Selected parameters for describing the dynamic characteristics of PEACT.

Structural layer	Response location	Response	Abbreviation
Rail	Top	Vertical acceleration	R_A2
		Vertical displacement	R_U2
Sleeper	Top	Vertical acceleration	S_A2
Surface layer	Top	Vertical acceleration	SL_A2
		Vertical stress	SL_S22
		Vertical displacement	SL_U2
DREAM blocks	Top	Vertical acceleration	AB_T_A2
		Vertical stress	AB_T_S22
		Vertical displacement	AB_T_U2
	Bottom	Vertical stress	AB_D_S22
		Vertical acceleration	AB_D_A2
		Lateral strain	AB_D_LE11
		Longitudinal strain	AB_D_LE33

3. Characterizing the dynamic responses of the transition zone

3.1. Influence of design parameters

Before analyzing the distribution of dynamic responses within the transition zone, it is essential to recognize that material variations strongly influence these responses. Additionally, the positional effect of each cross-section—arising from its proximity to boundaries and the material properties of adjacent DREAM blocks—also affects its dynamic behavior. Therefore, the effect of CR on the dynamic response was first investigated using model M-I, as shown in Fig. 9.

As illustrated in Fig. 9(a), the accelerations of all track components decrease with increasing CR content, indicating that CR effectively mitigates vibration transmission throughout the structure. The most significant reduction occurs when CR increases from 0 % to 2 %, after which the improvement diminishes, suggesting a saturation effect. While higher CR contents continue to reduce acceleration, they also lower structural stiffness and increase deformation, potentially aggravating unevenness in the transition zone. Hence, additional parameters beyond acceleration should be considered for a comprehensive evaluation.

As shown in Fig. 9(b), both track stiffness and vertical stress at the top of the DREAM blocks decrease markedly as CR content increases, confirming that CR softens the track structure under equivalent loads. In contrast, stresses in the surface layer change only slightly, indicating that DREAMs absorb most of the load, thereby protecting the substructure. Nevertheless, even for EA-6 CR, which exhibits the highest strain, the maximum bottom strain remains below 30 με, far below the control limit from the dynamic modulus tests (~180 με). This demonstrates that the DREAMs absorb stress effectively to protect the substructure and maintain favorable working conditions, meeting the dynamic response requirements for high-speed train loading conditions.

Regarding vertical displacement (Fig. 9(c)), the overall trend shows a reduction as CR content increases. This occurs because CR particles act as numerous micro-springs within the asphalt mixture, distributing deformation more evenly across the structure. Consequently, vertical displacement transmitted to the surface layer remains nearly constant across different CR contents, averaging around 0.47 mm.

3.2. Stress distribution

Previous studies have shown that the direction of train travel has minimal influence on the magnitude of dynamic responses in transition zones, and the responses on both sides of a bridge are nearly symmetric about the bridge axis [11]. Therefore, only Section 3 in Fig. 2(b) is analyzed to characterize the responses in the transition zone. The train speed is set to 350 km/h, and the simplified moving-load model is described in Appendix A.2. The asphalt blocks are arranged in a 10–20–10–10 pattern, consisting of 10 EA-6 CR blocks at the normal track end, followed by 20 EA-4 CR, 10 EA-2 CR, and 10 EA-0 CR blocks near the bridge end (Fig. A.1). For each type of DREAM block, the dynamic response is evaluated at the midsection, using the average response of two adjacent blocks as the representative value.

As shown in Fig. 10(a), the vertical stress at the top of the DREAM blocks increases and then decreases as the train passes, with a slight phase lag due to the viscoelasticity of DREAMs. For example, in the EA-6 CR section, the train passes at 0.024 s, while the stress peak appears at 0.026 s. After the train leaves, residual stress remains, indicating hysteretic recovery behavior. The maximum stress amplitude (214.41 kPa) occurs in the EA-0 CR section, while the minimum (77.70 kPa) occurs in the EA-6 CR section, confirming that higher CR content effectively reduces stress transmission and enhances structural protection.

At the surface layer, stress differences between sections become negligible (with all absolute values around 50 kPa, as indicated in Fig. 10(b)), demonstrating that DREAMs efficiently dissipate and redistribute loads. This stress level complies with the relevant standard

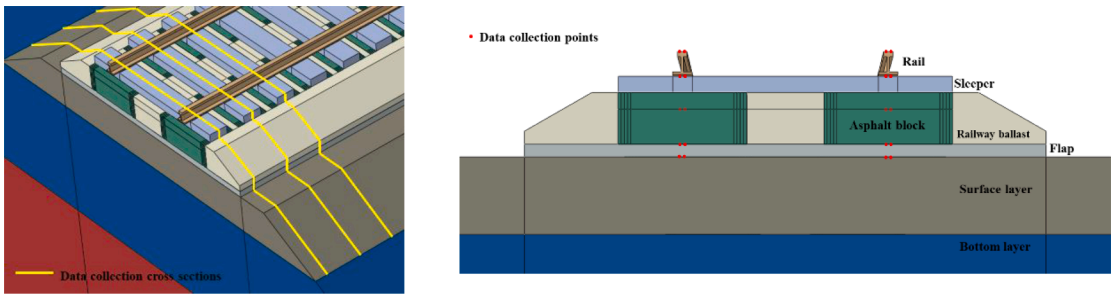

Fig. 8. Schematic of (a) data collection cross-sections, and (b) data collection points in a typical cross-section.

[46] and confirms that stress irregularities are confined within the DREAM layer, while the surface layer maintains a smooth and uniform stress distribution, validating PEACT's effectiveness in mitigating dynamic response irregularities in the transition zone.

In addition to examining the time-domain characteristics of specific cross-sections, this study also analyzed the lateral distribution of vertical stress within the PEACT structure. In Fig. 11(a) and Fig. 11(b), the DREAM block regions correspond to 0–1 m and 1.6–2.6 m, respectively, while Fig. 11(c) represents the surface layer. The stress values correspond to the moment when the train load is positioned directly above the analyzed cross-section.

As illustrated in the Fig.s, stress levels decrease with increasing CR content within the DREAM materials, consistent with the results of the time-domain analysis. For each cross-section, the lateral stress distribution is symmetric about the centerline, but it differs in shape across the layers. At the top of the DREAM blocks (Fig. 11(a)), the vertical stress exhibits a saddle-shaped pattern, with higher values near the sides and lower values at the center. The maximum compressive stress occurs directly beneath the train load, while the surrounding areas experience reduced compression and even localized tensile stresses near the block edges.

This tensile region arises because the upper surface of the block bends concave downward under the concentrated load, producing tension near the edges and compression at the center. At the outermost edge, which is directly in contact with the ballast, the vertical strain is nearly zero due to the weak vertical support of the granular ballast and the potential for local separation, resulting in a natural decay of stress toward zero at the edge. At the bottom of the DREAM blocks (Fig. 11(b)), the overall stress distribution remains similar, but the tensile zone shifts outward toward the block edges. This behavior results from the strong constraint provided by the rigid PCC grooves at the bottom, which causes deformation incompatibility between the viscoelastic DREAM block and the groove. The combined effect of vertical compression and shear transfer generates tensile stresses at the outer bottom edges, indicating a tendency for slight separation between the block and the groove.

In contrast, the surface layer (Fig. 11(c)) shows an entirely compressive stress distribution without any uplift tendency. The stress pattern remains saddle-shaped, with the peak directly under the train load and a secondary compressive ridge near the block edges. This difference arises because the surface layer is continuous and laterally constrained, which inhibits local bending or tension development. Meanwhile, the discrete geometry and lower lateral stiffness of the embedded DREAM blocks lead to localized deformation and stress concentration.

Overall, these findings demonstrate that while the PEACT effectively reduces vertical stress levels, the uplift behavior and edge tensile stresses of the DREAM blocks represent unique mechanical characteristics governed by boundary conditions, stiffness contrast, and deformation compatibility, which should be carefully considered in detailed design.

3.3. Strain distribution

Fig. 12(a) and Fig. 12(b) show the time-domain strain distribution at the bottom of the DREAM blocks. The lateral strain is slightly higher than the longitudinal strain, and both increase with higher CR content. Even at their maximum levels, the strain values remain low: the maximum lateral and longitudinal strains are 28.05 με and 25.47 με, respectively, both well below those observed in dynamic modulus tests (exceeding 300 με at 25 °C and 1 Hz). Under a 350 km/h train load, the DREAM blocks therefore operate within the linear elastic range without structural damage.

The peak strain response occurs with a delay relative to the train load, and this delay becomes more pronounced as the CR content increases. In the EA-6 CR section, approximately 15 με of lateral strain and 7 με of longitudinal strain remain after the train leaves the transition zone, while the longitudinal strain gradually increases under subsequent loads. Although the cumulative strain under repeated loading requires further evaluation, previous studies [12,22,23] indicate that the long-term performance of the DREAM blocks satisfies engineering requirements.

In terms of the lateral distribution of strain within the asphalt blocks, Fig. 13(a) and Fig. 13(b) show that the localized lateral strain peaks occur at the block edges, whereas the central region exhibits a broader elevated strain field caused by the bending of the block as a whole. However, since the strain levels remain below 30 με, this tendency is negligible, and the DREAM blocks continue to operate within a linear range without degradation in mechanical performance. In contrast, the longitudinal strain exhibits a different trend, with higher levels at the edges and lower levels at the center. The maximum longitudinal strain at the edges approaches 180 με, indicating that deformation in the longitudinal direction is more pronounced under vehicle loads. However, based on previous studies on the lateral resistance of PEACT [24], the strain levels in the DREAM blocks still within the linear range. Thus, the blocks are also capable of meeting the lateral resistance requirements of the track structure. It is worth noting that this value is still far below the typical tensile fatigue thresholds of epoxy–asphalt mixtures (approximately 330 με [39]), suggesting that the long-term risk of fatigue is minimal.

3.4. Displacement distribution

To capture the overall deformation characteristics of the PEACT, this study analyzed the displacement features of its components, as shown in Fig. 14. Overall, the peak vertical displacement across the transition zone components exhibits minimal variation, indicating that the deformation properties of DREAMs are nearly uniform and effectively protect the sub-structure. Given that train loads are high-frequency dynamic loads, the vertical displacement of the rail exhibits significant variability over time, as demonstrated in Fig. 14(a). However, due to the damping effects provided by the fasteners and DREAM blocks, this vibration effect is substantially attenuated before it impacts the substructure, as shown

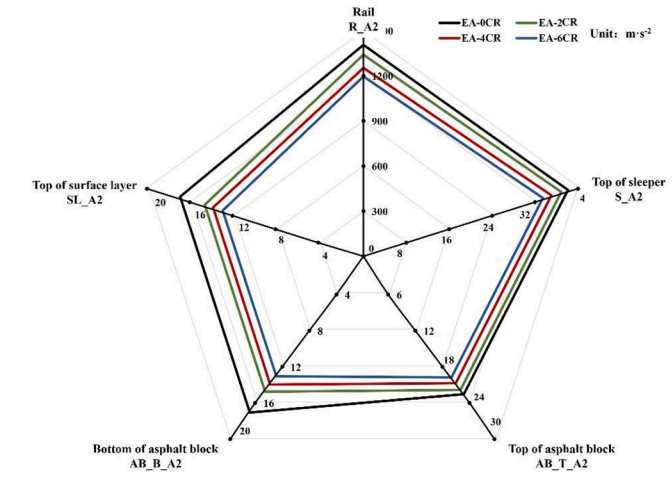

(a)

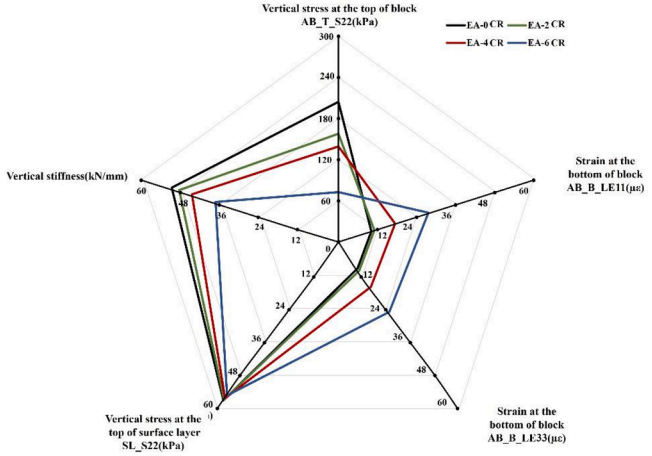

(b)

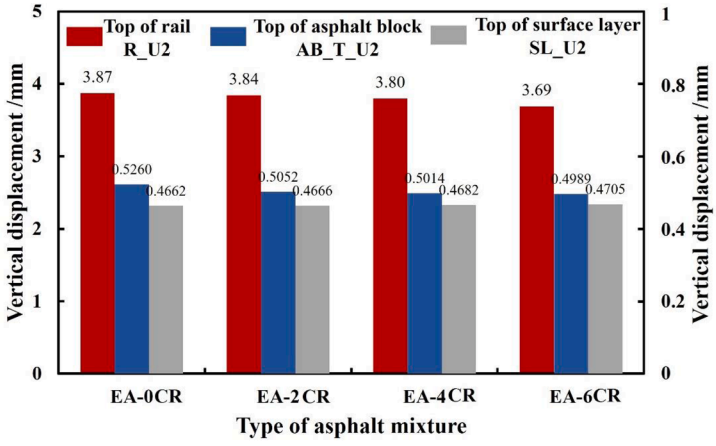

(c)

Fig. 9. Effect of rubber content on (a) vertical accelerations, (b) vertical stress, strain, stiffness, and (c) displacement.

in Fig. 14(b) and Fig. 14(c).

Despite the application of viscous boundary conditions, boundary effects are still evident in the computed vertical displacements. These effects are particularly noticeable in Fig. 14(b) and Fig. 14(c), where the displacement does not immediately return to zero after the train passes, but instead oscillates around zero for a period before stabilizing. For example, in the EA-6 CR section at the surface layer, three distinct oscillations occur after the load has passed, leading to a slight overestimation of vertical displacement. Moreover, as the rubber content increases, the oscillations become more pronounced and persist longer,

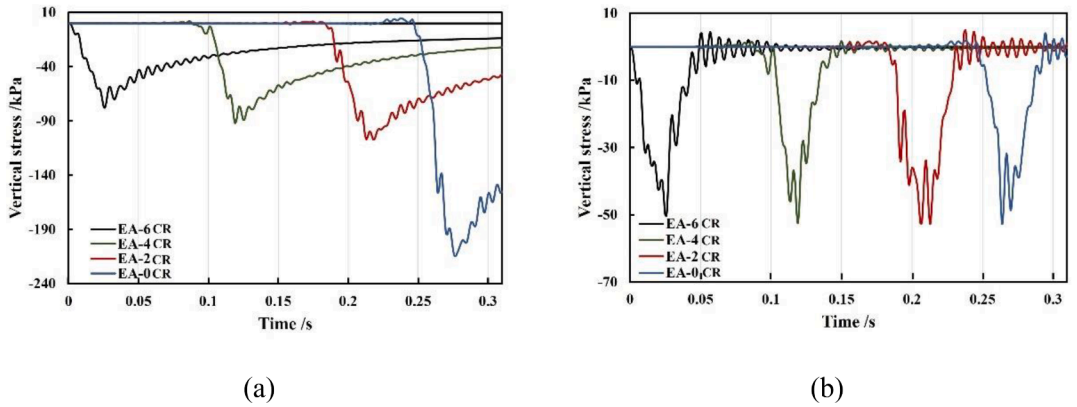

Fig. 10. Vertical stress characteristics at the top of asphalt blocks (a) AB_T_S22, and the top of the surface layer (b) SL_S22.

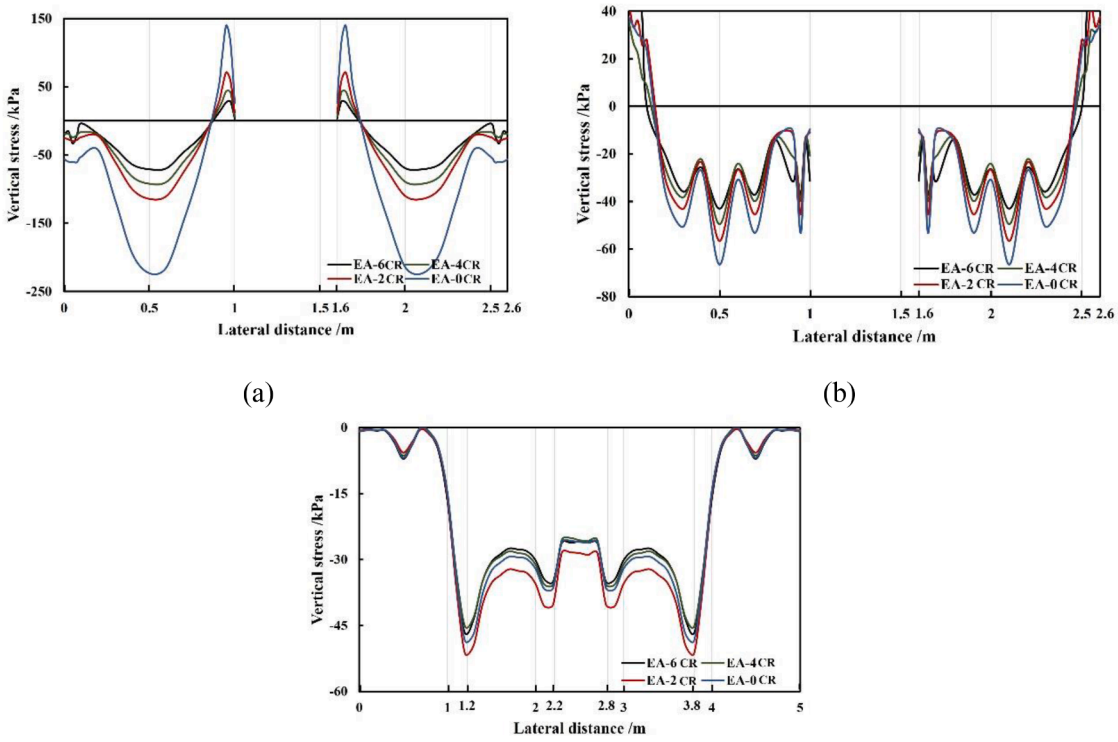

Fig. 11. Lateral distribution of vertical stress at (a) the top of blocks (AB_T_S22), (b) the bottom of blocks (AB_D_S22), and (c) the top of the surface layer (SL_S22).

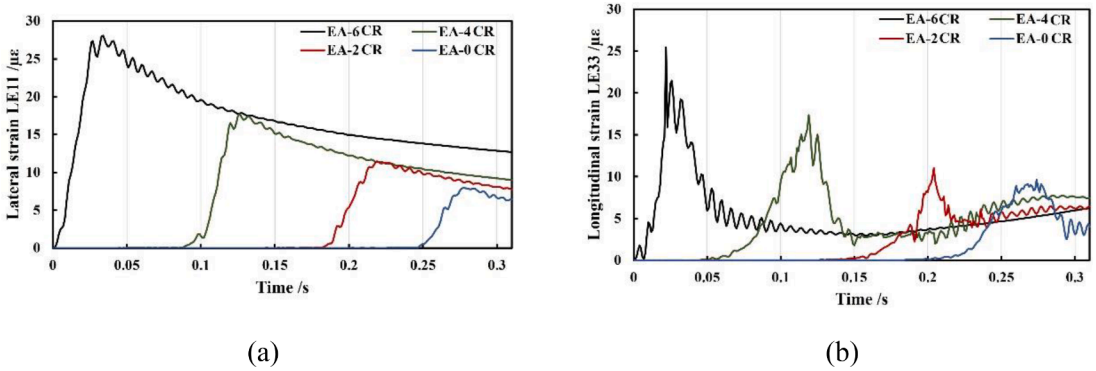

Fig. 12. Strain characteristics at the bottom of asphalt block (a) AB_D_LE11, and (b) AB_D_LE33.

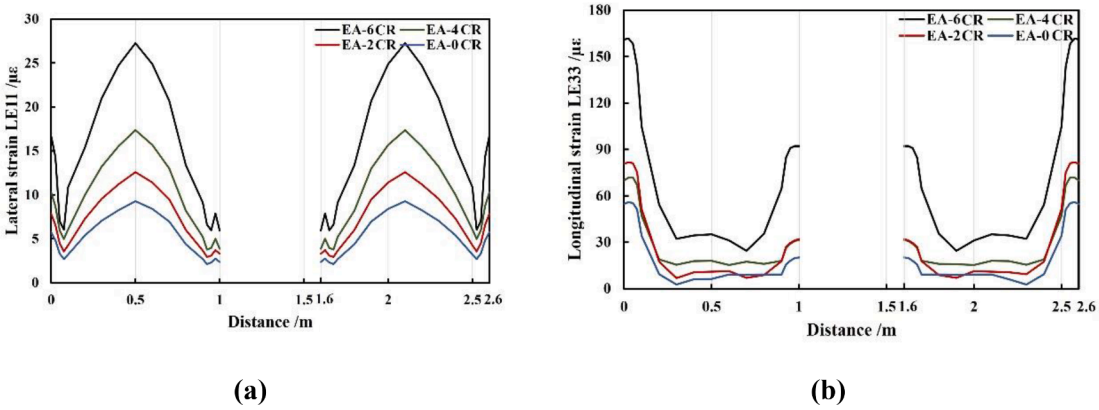

Fig. 13. Lateral strain distribution of (a) the lateral strain at the bottom of asphalt blocks (AB_D_LE11), and (b) the longitudinal strain at the bottom of asphalt blocks (AB_D_LE33).

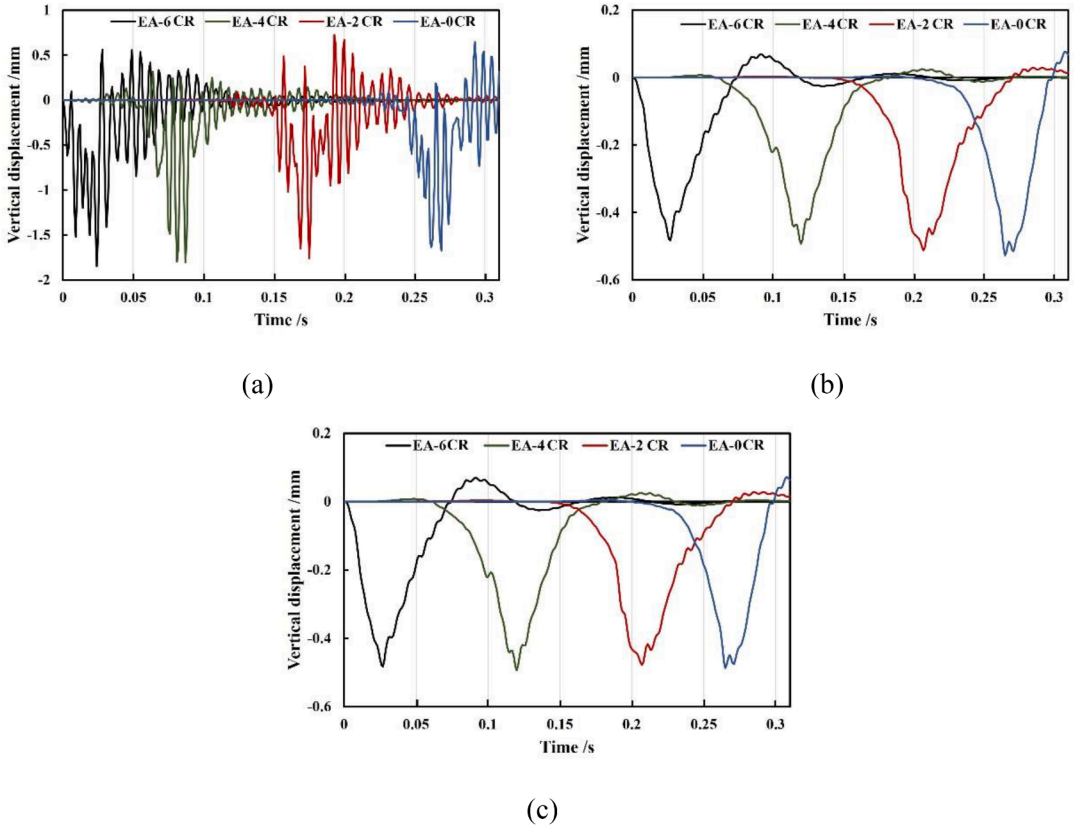

Fig. 14. Vertical displacement characteristics at the top of rail (a) R_U2, the top of asphalt blocks (b) AB_T_U2, and the top of surface layer (c) SL_U2.

further amplifying this overestimation. Nevertheless, even under these conditions, the maximum vertical displacement of the surface layer remains below 0.5 mm, indicating that deformation in the PEACT transition zone is minor and has a negligible impact on its dynamic performance, fully satisfying engineering requirements.

It is noted that the vertical displacement time histories at the top of the DREAM block and at the top of the surface layer are nearly identical, with differences less than 0.1 %. This indicates that both layers deform synchronously under vertical train loading. This behaviour is expected, because the two layers exhibit comparable vertical stiffness, resulting in negligible relative movement and a highly coordinated deformation response.

To examine the vertical displacement distribution within each PEACT component, the lateral displacement profiles at three positions aare analyzed, as shown in Fig. 15. Owing to the narrow cross-section of the rail, Fig. 15(a) includes only displacement data along the rail centerline, corresponding to lateral positions of 0.036 m and 1.636 m.

The results show that vertical displacement in all components increases slightly with higher CR content, although the increase is negligible relative to the overall displacement magnitude. This minor rise is attributed to the softening effect of CR, which enhances the deformability of the DREAMs and leads to marginally greater deformation under identical loading conditions. Nevertheless, as indicated by dynamic modulus test results [11], all DREAMs possess sufficiently high stiffness, resulting in minimal overall deformation.

Regarding lateral variation, the vertical displacement at the top of the DREAM blocks gradually increases from the edges toward the center. This occurs because the double-block prefabricated design allows both

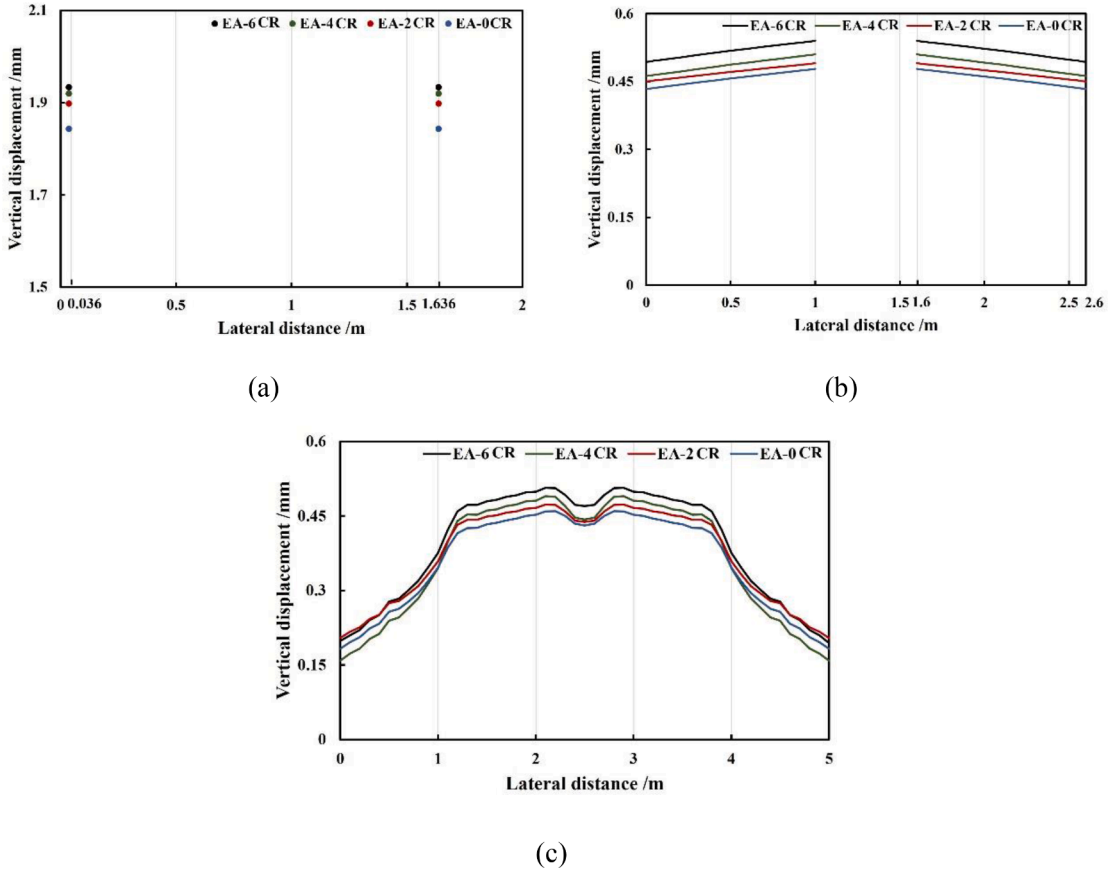

Fig. 15. Lateral distribution of vertical displacement at (a) the top of rail (R_U2), (b) the top of asphalt blocks (AB_T_U2), and (c) the top of surface layer (SL_U2).

blocks to share the train load, with load superposition being more pronounced near the centerline. In contrast, at the surface layer, the displacement at the center is slightly smaller than that above the asphalt blocks, forming a shallow depression, as shown in Fig. 15(c). This is because displacement in the surface layer is primarily driven by loads transmitted through the DREAM blocks, while regions away from direct load paths, such as the section centerline and edges, experience smaller vertical displacements.

3.5. Acceleration distribution

To evaluate the vibration attenuation performance of the DREAMs, the acceleration characteristics of various PEACT components are analyzed, as shown in Fig. 16. These Fig.s present acceleration responses in both the time and frequency domains. Overall, as the rubber content increases, the peak vertical vibration acceleration of the transition section decreases. The highest acceleration is observed at the EA-0 CR section (Fig. 16(a1)), reaching 1387.05 m·s^{-2}, which satisfies the Technical Regulations for Dynamic Acceptance of High-Speed Railways [47] concerning passenger comfort during operation.

The results show that the maximum absolute vertical acceleration obtained from the model is well below the regulatory limits of 500 g for ballastless tracks and 300 g for ballasted tracks [47], indicating that the predicted response levels fall within the safe operational range for high-speed railway applications. These results also demonstrate that the incorporation of DREAMs and CR-modified mixtures leads to improved vibration attenuation along the transition zone without inducing excessive deformation in the rail or upper structural layers. This confirms that the PEACT system maintains structural stability and smooth load transfer even in its softened state, further supporting the suitability of DREAMs for transition-zone applications in high-speed rail.

At the top of the DREAM blocks and within the surface layer, similar attenuation trends are observed, though with smaller magnitudes. The maximum vertical accelerations are 22.75 m·s^{-2} and 20.04 m·s^{-2}, respectively, indicating that the fastening systems and DREAM blocks efficiently dissipate vibrations, keeping acceleration levels in lower layers well within high-speed railway design requirements.

Frequency-domain analyses further confirm that higher CR content reduces the influence of vibration loads on the PEACT. As the CR content increases, the acceleration spectra become increasingly concentrated within specific low-frequency bands rather than distributed across a broad frequency range. This difference is particularly evident between the spectra of EA-0 CR and EA-2 CR at the rail. At the DREAM block and surface layer levels, the fastening system and DREAMs further smooth the spectra, concentrating dominant vibration frequencies below 20 Hz. These results demonstrate that the PEACT transition zone exhibits excellent vibration attenuation characteristics and maintains structural integrity under high-frequency train-induced vibration.

To further illustrate the attenuation of vertical acceleration across structural layers, the peak values from the time-history curves of vertical acceleration at various locations are extracted for four cross-sections, and the corresponding attenuation curves are plotted, as shown in Fig. 17. The results show that the attenuation of vertical acceleration along the trackbed generally follows an exponential decay pattern, with the fitted equations and coefficients of determination (R^2) provided in the upper-right corner of Fig. 17.

The fitted curves indicate that most acceleration attenuation occurs between the rail and the top of the sleeper, primarily due to the damping effect of the fastening system. The attenuation rate in this region exceeds 95 % across all cases. However, even after attenuation, the minimum vertical acceleration at the sleeper top remains relatively high at 33.45 m·s^{-2}. Without additional vibration-damping capability in the

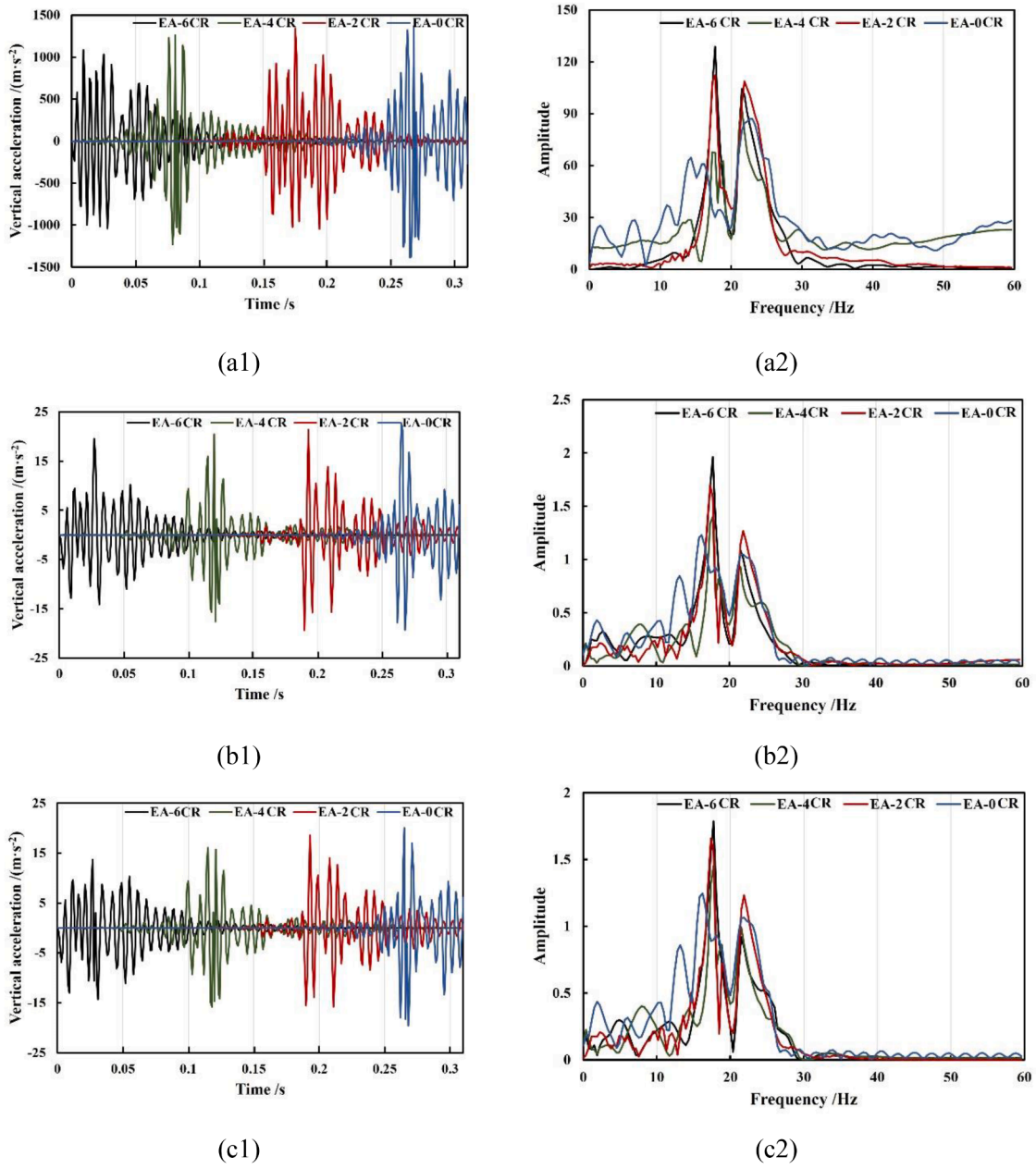

Fig. 16. Vertical acceleration characteristics at the top of rail (a1) R_A2 time-domain, (a2) R_A2 frequency-domain, at the top of asphalt blocks (b1) AB_T_A2 time-domain, (b2) AB_T_A2 frequency-domain, and at the top of surface layer (c1) SL_A2 time-domain, (c2) SL_A2 frequency-domain.

substructure, such high levels could potentially damage the surface layer. The results confirm that the DREAMs effectively mitigate this issue. When vibrations propagate to the DREAM blocks, the vertical acceleration decreases by 44.57 %, 41.63 %, 39.30 %, and 37.66 % for the four sections, respectively, reducing the acceleration to below 25 $m{\cdot}s^{-2}$ and providing substantial protection for the lower layers.

Furthermore, the attenuation improves with higher CR content, demonstrating that the inclusion of CR significantly enhances vibration reduction within the trackbed. Incorporating CR into the viscoelastic asphalt mixture increases its elasticity, improving overall vibration absorption. As vibrations propagate further downward through the PCC grooves to the surface layer, the vertical acceleration falls below 20 $m{\cdot}s^{-2}$. However, the attenuation rate from the bottom of the DREAM blocks to the surface layer is only about 6 %, underscoring the critical role and necessity of the DREAMs in achieving effective vibration mitigation within the PEACT transition zone.

4. Discussions

4.1. Further improvement of the present work

This study aims to provide a comprehensive and accurate description of the dynamic response characteristics of the PEACT transition zone. However, due to the limitations of the computational methods and related factors, the numerical model and analysis methods employed in this work still have room for improvement. This section briefly discusses these issues.

4.1.1. Accuracy of lateral stress analysis

In the modeling process, the actual contact characteristics between the DREAM block and the filled ballast are not considered. The contact between the DREAM block and the ballast is represented by Coulomb friction, which does not accurately represent the real contact conditions. Furthermore, the FEM simplified the ballast as an isotropic

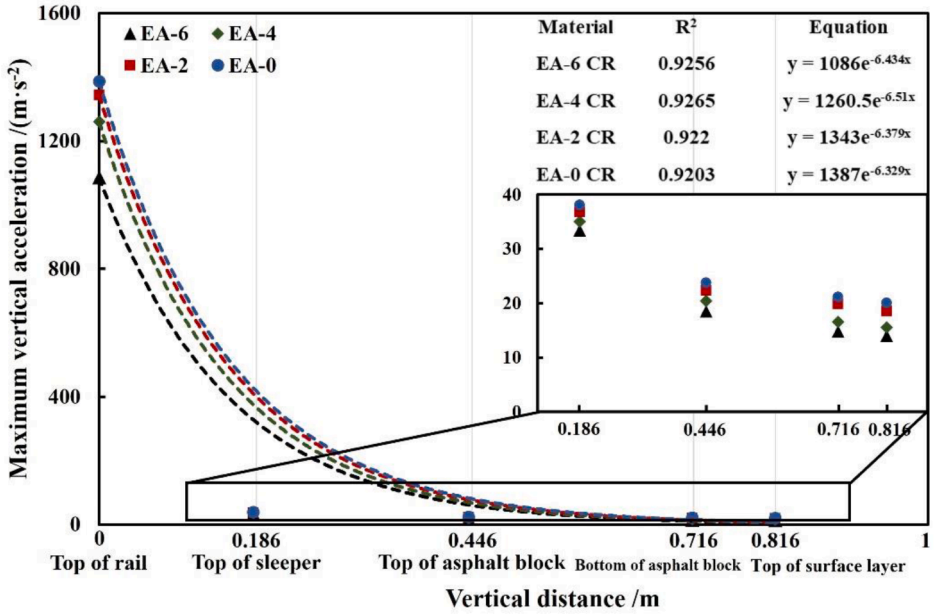

Fig. 17. Attenuation scheme of maximum vertical acceleration among track structures.

homogeneous material, which fails to capture the true mechanical characteristics of the ballast. As a result, although the numerical model in this study is verified in the vertical direction, its accuracy in the lateral and longitudinal directions remains questionable. This is particularly evident when analyzing the lateral distribution of the vertical stress AB_D_S22 of the DREAM block, as shown in Fig. 11(b). It can be observed that in the DREAM block region, especially in the groove area illustrated in Fig. 11(a), the stress results between adjacent elements vary significantly, in stark contrast to the smooth stress distribution observed at the top of the DREAM block in Fig. 11(a). This discrepancy suggests that the computed lateral stresses within the DREAM block may be unstable due to lateral contact effects. Another potential cause of this phenomenon is the relatively coarse lateral mesh density of the DREAM block. As shown in Fig. 6(a) and Fig. 6(b), the mesh sensitivity analysis considered only the convergence of numerical results while overlooking stability.

To address this issue, several studies have used discrete element methods (DEM) to analyze the mechanical performance of polyurethane track beds with structures similar to PEACT, achieving promising results [17]. However, DEM models are similarly constrained by computational efficiency and are unable to simulate the dynamic response characteristics of long sections, such as the 90 m track transition modeled in this study.

4.1.2. *Shape effect of asphalt blocks*

In general, irregular geometries not only reduce model convergence but also significantly increase computational complexity. In this study, the presence of grooves in the asphalt block, as shown in Fig. 1(a), leads to highly complex internal contact conditions within the model, severely affecting computational efficiency. Furthermore, the mismatch between the mesh nodes of the DREAM block and those of the ballast, sleeper, and groove layer further reduces computational efficiency and may cause stress concentration at the edges of the asphalt block. This implies that during the analysis of the lateral stress distribution in the DREAM block, edge stresses might be overestimated, as shown in Fig. 11(a) and Fig. 11(b).

In Fig. 11(a), the maximum stress in the EA-6 CR section reaches nearly 150 kPa, occurring at the edge of the asphalt block near the inner side of the rail. Although this edge does not directly bear the train load transmitted through the sleeper, its stress magnitude is only 100 kPa lower than the central region of the DREAM block. Thus, the accuracy of these results at the edge requires further validation. Additionally, as shown in Fig. 11(a) and Fig. 11(b), the stress distribution indicates that some regions of the DREAM block are under tension while others are under compression, with differing stress patterns between the top and bottom surfaces. This type of loading could lead to damage in the asphalt block during its service life, underscoring the need for further validation of its stress characteristics.

4.2. *Optimal material-structure composition*

Another noteworthy aspect of this study is its focus on analyzing the dynamic response characteristics of DREAMs when applied in the PEACT transition zone. Most results indicate that DREAMs exhibit excellent applicability. However, for transition zones of the trackbed, their primary purpose is to achieve a smooth variation in dynamic responses along the longitudinal direction. Previous research [11] has demonstrated that, compared to polyurethane trackbeds, which is already in practical use, a specific DREAMs configuration of 10–20–10–10 achieves smoother dynamic response transitions in the transition zone and offers significant advantages, as shown in Fig. 18.

Nevertheless, for the PEACT structure, both the sequence and total number of DREAMs significantly affect the overall variation trend shown in Fig. 18, even though the time-history and lateral response patterns of individual DREAM block sections remain largely consistent. Since the primary goal of transition zone design is to maintain continuous and smooth dynamic behavior along the longitudinal direction, exploring various combinations and arrangements of DREAMs to determine the optimal configuration will be a key focus of future research.

5. Conclusions

This study presents a comprehensive numerical characterization of the dynamic behavior of the PEACT transition zone, focusing on how DREAMs' gradation influences stress, strain, displacement, and vibration transmission within the structure. A refined and validated full-scale 3D FE model is established and validated with optimized boundary conditions, mesh size, and material parameters. The dynamic response of the PEACT transition zone with the DREAM arrangement scheme

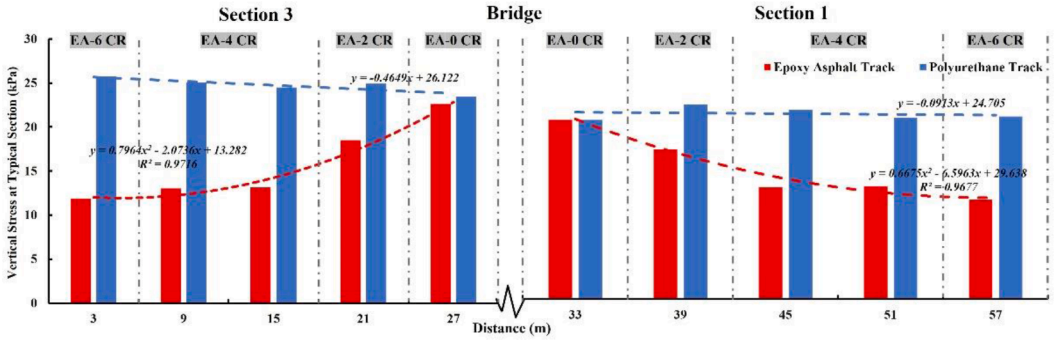

Fig. 18. Schematic of the longitudinal distribution of vertical stress (taking SL_S22 as an example), and comparison between PEACT and polyurethane track bed.

10–20–10–10 under high-speed train loading is quantified. The main findings and conclusions of this study are listed as follows:

- The optimal boundary condition and mesh size of PEACT transition zone modelling is selected: viscous boundaries are identified as providing the most stable early-phase responses among the compared options, while key response measures are found to change by < 6 % when refining critical layers from 0.10 m to 0.05 m, leading to the use of 0.10 m elements in critical parts for a balanced accuracy–efficiency trade-off.
- Under 350 km/h train loading, vertical stresses at DREAM tops are highly dependent on rubber content (e.g., $\approx$ 214.41 kPa at EA-0 CR and $\approx$ 77.70 kPa at EA-6), whereas surface-layer stresses remain clustered near $\approx$ 50 kPa and within limits, evidencing effective load redistribution by DREAMs.
- The strains at the bottom of DREAM blocks are kept low in time histories (peaks $\approx$ 28.05 με lateral, $\approx$ 25.47 με longitudinal), remaining well below dynamic modulus control threshold. The linear viscoelastic operation of DREAM blocks is therefore indicated for the studied conditions.
- Vertical displacements in the PEACT transition zone are kept small and observed to be synchronized between the top of DREAM blocks and the surface layer (difference $<$0.1 %), with surface-layer maxima $<$ 0.5 mm. Minor post-pass oscillations are attributed to residual boundary effects.
- Layered vibration attenuation is quantified in PEACT transition zone: rail-to-sleeper peak vertical acceleration is reduced by $>$ 95 % (fastener damping), with a further 37.66–44.57 % reduction across DREAMs to $<$ 25 m/s^2 at block levels and $<$ 20 m/s^2 at the surface layer.
- Rail vibrations in the hardest section (EA-0 CR) reached $\approx$ 1387.05 m/s^2 (remaining below regulatory caps when expressed in g), and are shown to decrease with higher CR content. Dominant frequencies at deeper layers are concentrated below 20 Hz.

In conclusion, the findings support the broader application of PEACT with DREAMs in high-speed railway infrastructure, offering a promising solution to the challenges of dynamic response management in transition zones. The study contributes to the design and implementation of advanced track systems, paving the way for safer, more reliable, and comfortable high-speed rail transport.

Declaration of AI use

During the preparation of this work, the authors utilized ChatGPT 5.1 Plus to enhance the readability of the entire paper. The authors reviewed and edited the content and take full responsibility for the publication.

CRediT authorship contribution statement

You Wu: Writing – review & editing, Writing – original draft, Visualization, Validation, Methodology, Investigation, Formal analysis, Data curation, Conceptualization. **Chenguang Shi:** Writing – review & editing, Writing – original draft, Supervision, Investigation, Funding acquisition. **Yunhong Yu:** Writing – review & editing, Writing – original draft, Conceptualization. **Yulou Fan:** Writing – review & editing, Writing – original draft, Conceptualization. **Jun Yang:** Writing – review & editing, Writing – original draft, Supervision, Funding acquisition, Conceptualization.

Declaration of competing interest

The authors declare that they have no known competing financial interests or personal relationships that could have appeared to influence the work reported in this paper.

Acknowledgment

The authors acknowledge the financial support of the National Natural Science Foundation of China (No. 52508484, No. 52078130, No. 52378444), the Natural Science Foundation of Chongqing (CSTB2025NSCQ-GPX0872), China Postdoctoral Science Foundation under Grant Number (2025MD774152).

Appendix A. Equations of the PEACT model

A.1. Track model

The dynamic model of the PEACT using DREAMs in the transition zone is shown in Fig. A.1(a) and Fig. A.1(b), respectively, where Fig. A.1(a) is the mechanic model and Fig. A.1(b) is the application form for DREAMs. For simplicity, some of the DREAM blocks are omitted from the Fig.s, and some of the viscoelastic units in each block. The equation of motion for this model can be expressed using Eq. (A.1).

$$M\ddot{u} + C\dot{u} + Ku = P \tag{A.1}$$

where $\boldsymbol{M}$, $\boldsymbol{C}$, and $\boldsymbol{K}$ are mass, damping, and stiffness matrices of the structure, respectively. $\ddot{u}$, $\dot{u}$, and u are acceleration, velocity, and displacement

vectors, respectively. ***P*** is the train load force vector, and the definition for ***P*** in M-I and M-II can be seen in section A.2.

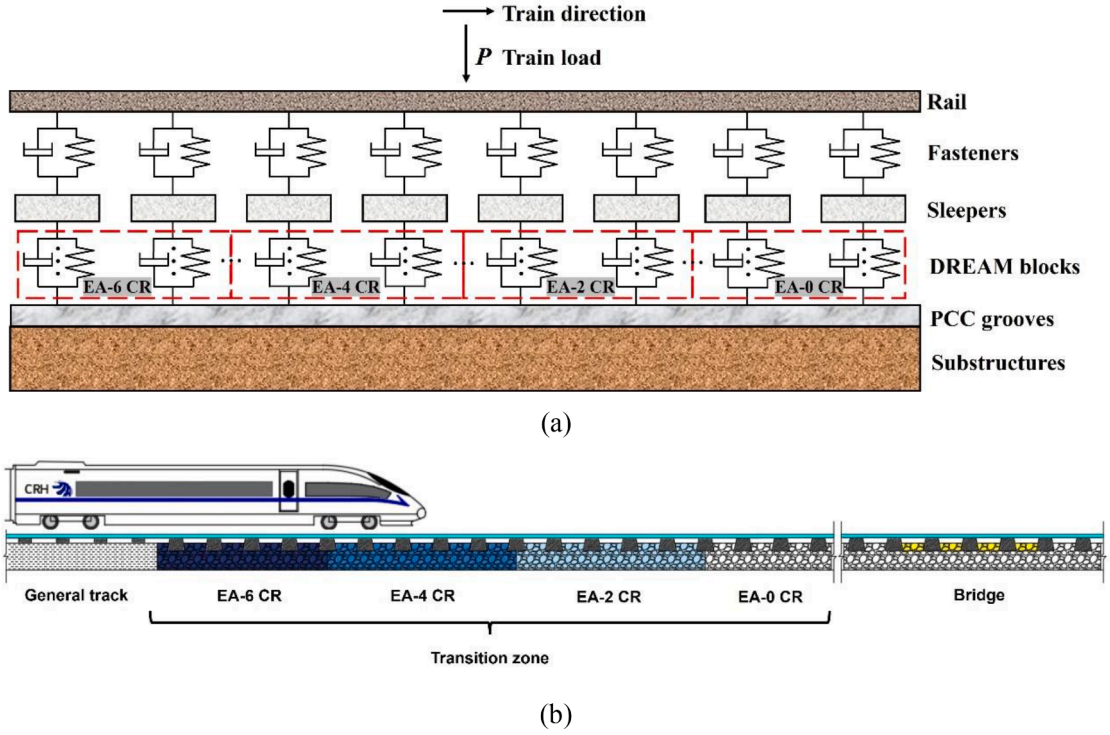

Fig. A.1. The dynamic model of the PEACT transition zone (a) mechanic model, and (b) application forms of DREAMs.

A.2. Train load

For the single wheel load applied to M-I, it can be approximated using Eq. (A.2):

$$P = P_0 A e^{-\frac{(vt)^2}{2w^2}} \tag{A.2}$$

where P_0 is the axle load of the train vehicle, v is the train speed, t is the loading time, A and w are fitting parameters. For normal ballasted track, the proportion of five sleepers is usually set as 0.1:0.2:0.4:0.2:0.1[49], and under this condition, Eq. (A.2) can be written as:

$$P = 0.36 P_0 e^{-\frac{(vt)^2}{0.78}} \tag{A.3}$$

For moving train load applied to M-II, three kinds of different excitation were considered in the simplification equations, respectively for simulating low-frequency vibrations (train vehicles), mid-frequency vibrations (unsprung mass), and high-frequency vibrations (train-track interactions and irregularities):

$$F(t)' = P_0 + P_1 \sin\omega_1 t + P_2 \sin\omega_2 t + P_3 \sin\omega_3 t \tag{A.4}$$

where $F(t)'$ is the train load. P_0 is the static load of the train vehicle. $P_i (i = 1,\ 2,\ 3)$ is the vibration load for the typical frequency range and $\omega_i (i = 1,\ 2,\ 3)$ is the corresponding frequency. ω_i can be calculated using Eq. (A.5):

$$\omega_i = \frac{2\pi v}{L_i} \tag{A.5}$$

where v is the train speed, L_i is the wavelength for each excitation. Taking the CRH3 train, which has been widely used in China and is also applied in this study, as an example, its axle load is 17,000 kg, the upsprung mass M_0 is 750 kg, thus P_i for the CRH3 train can be expressed as:

$$P_i = M_0 a_i \omega_i^2 \tag{A.6}$$

where $L_1 = 10\ m,\ a_1 = 3.5\ mm; L_2 = 2\ m,\ a_2 = 0.4\ mm; L_3 = 0.5\ m,\ a_3 = 0.08\ mm$, respectively for corresponding wavelength and vector heights.

Subsequently, the sleeper distribution of train load was also considered in this simplification using correction coefficients k_1 and k_2, respectively, for the stacking effect of wheelsets and the sleepers distribution effects. Under this condition, the final equation of the moving train load is:

$$F(t) = k_1 k_2 F(t)' \tag{A.7}$$

where the value of k_1 and k_2 are 1.538 and 0.7, respectively.

A.3. Contact model

All contact in the established model is modeled using Penalty contact, as shown in Fig. A.2. During the calculating process, the penetration between the slave surface and master surface needs to be searched at each time step. When there is no penetration, no force is added. When the penetration is found, an additional force is added to resist and ultimately eliminate the penetration [29]. Under this condition, the additional force vector f_s can be expressed as:

$$f_s = -lk_i n_i, l < 0 \tag{A.8}$$

where l is the depth of penetration, n_i is a vector normal to the outside of the contact point, k_i is the stiffness of the master surface can be calculated as:

$$k_i = \frac{f_{si} K_i A_i^2}{V_i} \tag{A.9}$$

where f_{si} is the contact stiffness coefficient, K_i is the bulk modulus, A_i is the contact area, and V_i is contact volume.

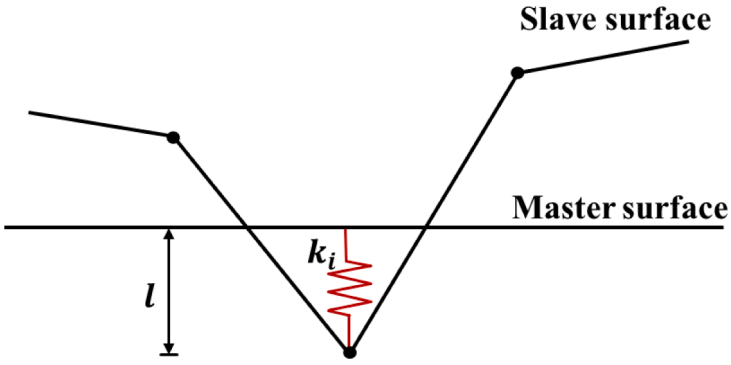

Fig. A.2. Schematic of Penalty contact.

Appendix B. Element matrix of the model

B.1. Timoshenko beam elements for rail and sleepers

The Timoshenko beam elements are employed to develop the rail and sleeper model [48]. Each element has two nodes and four degrees of freedom (DOFs). Its displacement vector $\boldsymbol{u}$ can be expressed as:

$$u = [\omega_1, \theta_1, \omega_2, \theta_2]^{\mathrm{T}} \tag{B.1}$$

where ω_1 and ω_2 are vertical degrees, and θ_1 and θ_2 are in-plane rotational degrees. Other degrees of elements were ignored.

For the rail and sleeper physical model, their element stiffness matrix $\boldsymbol{K}$ can be expressed as

$$K = \frac{EI}{(1+\phi)L^3}\begin{bmatrix} 12 & 6L & -12 & 6L \\ & (4+\phi)L^2 & -6L & (2-\phi)L^2 \\ & & 12 & -6L \\ \text{symmetric} & & & (4+\phi)L^2 \end{bmatrix} \tag{B.2}$$

where L is element length, E is Young's modulus, and I is the area moment of inertia of the cross-section. ϕ can be calculated using Eq. (B.3):

$$\phi = \frac{12}{L^2}\left(\frac{EI}{\kappa GA}\right) \tag{B.3}$$

where κ is the shear coefficient, G is shear modulus, A is the area of cross-section.

The mass matrix of the Timoshenko element can be expressed as

$$M = \boldsymbol{M}^{\boldsymbol{pA}} + \boldsymbol{M}^{\boldsymbol{pI}} \tag{B.4}$$

where $\boldsymbol{M}^{\boldsymbol{pA}}$ is related to translational inertia:

$$\boldsymbol{M}^{\rho A}=\frac{\rho AL}{210(1+\phi)^2}\begin{bmatrix} 70\phi^2+147\phi+78 & \left(35\phi^2+77\phi+44\right)\frac{L}{4} & 35\phi^2+63\phi+27 & -\left(35\phi^2+63\phi+26\right)\frac{L}{4} \\ & \left(7\phi^2+14\phi+8\right)\frac{L^2}{4} & 35\phi^2+63\phi+26 & -\left(7\phi^2+14\phi+6\right)\frac{L^2}{4} \\ & & 70\phi^2+147\phi+78 & -\left(35\phi^2+77\phi+44\right)\frac{L}{4} \\ & \text{symmetric} & & \left(7\phi^2+14\phi+8\right)\frac{L^2}{4} \end{bmatrix} \tag{B.5}$$

and $\boldsymbol{M}^{\rho I}$ is related to rotational inertia:

$$\boldsymbol{M}^{\rho I}=\frac{\rho I}{30(1+\phi)^2L}\begin{bmatrix} 36 & -(15\phi-3)L & -36 & -(15\phi-3)L \\ & \left(10\phi^2+5\phi+4\right)L^2 & (15\phi-3)L & \left(5\phi^2-5\phi-1\right)L^2 \\ & & 36 & (15\phi-3)L \\ & \text{symmetric} & & \left(10\phi^2+5\phi+4\right)L^2 \end{bmatrix} \tag{B.6}$$

Besides, for the shape function ω and θ is Eq. (B.1), they can be expressed as

$$\boldsymbol{\omega}^{\mathrm{T}}=\begin{bmatrix} \frac{1}{(1+\phi)}\left\{2\left(\frac{x}{L}\right)^3-3\left(\frac{x}{L}\right)^2-\phi\left(\frac{x}{L}\right)+(1+\phi)\right\} \\ \frac{L}{(1+\phi)}\left\{\left(\frac{x}{L}\right)^3-\left(2+\frac{\phi}{2}\right)\left(\frac{x}{L}\right)^2+\left(1+\frac{\phi}{2}\right)\left(\frac{x}{L}\right)\right\} \\ -\frac{1}{(1+\phi)}\left\{2\left(\frac{x}{L}\right)^3-3\left(\frac{x}{L}\right)^2-\phi\left(\frac{x}{L}\right)\right\} \\ \frac{L}{(1+\phi)}\left\{\left(\frac{x}{L}\right)^3-\left(1-\frac{\phi}{2}\right)\left(\frac{x}{L}\right)^2-\frac{\phi}{2}\left(\frac{x}{L}\right)\right\} \end{bmatrix} \tag{B.7}$$

$$\boldsymbol{\theta}^{\mathrm{T}}=\begin{bmatrix} \frac{6}{(1+\phi)L}\left\{\left(\frac{x}{L}\right)^2-\left(\frac{x}{L}\right)\right\} \\ \frac{1}{(1+\phi)}\left\{3\left(\frac{x}{L}\right)^2-(4+\phi)\left(\frac{x}{L}\right)+(1+\phi)\right\} \\ -\frac{6}{(1+\phi)L}\left\{\left(\frac{x}{L}\right)^2-\left(\frac{x}{L}\right)\right\} \\ \frac{1}{(1+\phi)}\left\{3\left(\frac{x}{L}\right)^2-(2-\phi)\left(\frac{x}{L}\right)\right\} \end{bmatrix} \tag{B.8}$$

B.2. Spring-damper elements for fasteners

The spring-damper elements are employed to simulate the fastener system in the track structure. There is no mass matrix for these elements, and their stiffness matrix $\boldsymbol{K}$ and damping matrix $\boldsymbol{M}$ can be expressed as:

$$K=k\begin{bmatrix} 1 & 0 & -1 & 0 \\ & 0 & 0 & 0 \\ & & 1 & 0 \\ \text{symmetric} & & & 1 \end{bmatrix} \tag{B.9}$$

$$M=c\begin{bmatrix} 1 & 0 & -1 & 0 \\ & 0 & 0 & 0 \\ & & 1 & 0 \\ \text{symmetric} & & & 1 \end{bmatrix} \tag{B.10}$$

where k and c are the stiffness and damping values of fasteners, respectively.

Data availability

Data will be made available on request.

References

[1] W. contributors, China railway high-speed. https://en.wikipedia.org/w/index.php?title=China_Railway_High-speed&oldid=1229523167, 2024. Accessed 17 June 2024 20:53 UTC.

[2] M. Sol-Sánchez, G. D'Angelo, Review of the design and maintenance technologies used to decelerate the deterioration of ballasted railway tracks, Constr. Build. Mater. 157 (2017) 402–415, https://doi.org/10.1016/j.conbuildmat.2017.09.007.

[3] G. Jing, P. Aela, Review of the lateral resistance of ballasted tracks, Proc. Inst. Mech. Eng. F 234 (8) (2019) 807–820, https://doi.org/10.1177/0954409719866355.

[4] R. Sañudo, L. dell'Olio, J.A. Casado, I.A. Carrascal, S. Diego, Track transitions in railways: a review, Constr. Build. Mater. 112 (2016) 140–157, https://doi.org/10.1016/j.conbuildmat.2016.02.084.

[5] J. Deng, X. Liu, G. Jing, Z. Bian, Probabilistic risk analysis of flying ballast hazard on high-speed rail lines, Transp. Res. C 93 (2018) 396–409, https://doi.org/10.1016/j.trc.2018.06.003.

[6] G. Jing, D. Ding, X. Liu, High-speed railway ballast flight mechanism analysis and risk management – A literature review, Constr. Build. Mater. 223 (2019) 629–642, https://doi.org/10.1016/j.conbuildmat.2019.06.194.

[7] A.D. Quinn, M. Hayward, C.J. Baker, F. Schmid, J.A. Priest, W. Powrie, A full-scale experimental and modelling study of ballast flight under high-speed trains, Proc. Inst. Mech. Eng. F 224 (2) (2009) 61–74, https://doi.org/10.1243/09544097jrrt294.

[8] Y. Tong, G. Liu, K. Yousefian, G. Jing, Track vertical stiffness –Value, measurement methods, effective parameters and challenges: a review, Transp. Geotech. 37 (2022) 100833, https://doi.org/10.1016/j.trgeo.2022.100833.

[9] J. Choi, Influence of track support stiffness of ballasted track on dynamic wheel-rail forces, J. Transp. Eng. 139 (7) (2013) 709–718, https://doi.org/10.1061/(ASCE)TE.1943-5436.0000543.

[10] Z. Yu, D.P. Connolly, P.K. Woodward, O. Laghrouche, Settlement behaviour of hybrid asphalt-ballast railway tracks, Constr. Build. Mater. 208 (2019) 808–817, https://doi.org/10.1016/j.conbuildmat.2019.03.047.

[11] Y. Wu, C. Shi, Y. Yu, H. Chen, Y. Fan, H. Wang, J. Yang, W. Huang, Dynamic behavior of precast epoxy asphalt track bed for transition zone in high-speed railway: a numerical approach, Transp. Geotech. 40 (2023) 100960, https://doi.org/10.1016/j.trgeo.2023.100960.

[12] C. Shi, X. Sun, T. Wang, Y. Wu, S. Liu, H. Wang, J. Yang, Y. Xu, L. Qie, Numerical analysis of dynamic behavior of Bi-block precast asphalt trackbed for high-speed railway, Constr. Build. Mater. 342 (2022) 128088, https://doi.org/10.1016/j.conbuildmat.2022.128088.

[13] W. Yonggang, Optimal design scheme of prefabricated polyurethane curing track bed, Railw. Stand. Des. 66 (11) (2022) 58–62, https://doi.org/10.13238/j.issn.1004-2954.202108170006.

[14] K. Jadidi, M. Esmaeili, M. Kalantari, M. Khalili, M. Karakouzian, A review of different aspects of applying asphalt and bituminous mixes under a railway track, Mater. (1996-1944) 14 (1) (2021) 169, https://doi.org/10.3390/ma14010169. –169.

[15] M. Giunta, S. Bressi, G. D'Angelo, Life cycle cost assessment of bitumen stabilised ballast: a novel maintenance strategy for railway track-bed, Constr. Build. Mater. 172 (2018) 751–759, https://doi.org/10.1016/j.conbuildmat.2018.04.020.

[16] X. Xiao, J. Wang, D. Cai, L. Lou, F. Xiao, A novel application of thermoplastic polyurethane/waste rubber powder blend for waterproof seal layer in high-speed railway, Transp. Geotech. 27 (2021), https://doi.org/10.1016/j.trgeo.2020.100503.

[17] G. Jing, L. Qie, V. Markine, W. Jia, Polyurethane reinforced ballasted track: review, innovation and challenge, Constr. Build. Mater. 208 (2019) 734–748, https://doi.org/10.1016/j.conbuildmat.2019.03.031.

[18] Q. Xiang, F. Xiao, Applications of epoxy materials in pavement engineering, Constr. Build. Mater. 235 (2020), https://doi.org/10.1016/j.conbuildmat.2019.117529.

[19] H. Xie, C. Li, Q. Wang, A critical review on performance and phase separation of thermosetting epoxy asphalt binders and bond coats, Constr. Build. Mater. 326 (2022), https://doi.org/10.1016/j.conbuildmat.2022.126792.

[20] W. Huang, W. Guo, Y. Wei, Thermal effect on rheological properties of epoxy asphalt mixture and stress prediction for bridge deck paving, J. Mater. Civ. Eng. 31 (10) (2019) 04019222, https://doi.org/10.1061/(ASCE)MT.1943-5533.0002861.

[21] P. Mohan, A critical review: the modification, properties, and applications of epoxy resins, Polym. Plast. Technol. Eng. 52 (2) (2013) 107–125, https://doi.org/10.1080/03602559.2012.727057.

[22] C. Shi, H. Zhang, T. Wang, Y. Zhou, S. Liu, H. Wang, J. Yang, Y. Xu, L. Qie, Design and performance evaluation of Bi-block precast rubberized epoxy asphalt trackbed for railway, Constr. Build. Mater. 313 (2021) 125347, https://doi.org/10.1016/j.conbuildmat.2021.125347.

[23] Y. Wu, Y. Zhou, C. Shi, Y. Yu, Y. Fan, X. Cai, Y. Zhou, H. Wang, M. Gong, J. Hong, J. Yang, W. Huang, Interlayer bonding quality evaluation of sleeper-asphalt block composite structure applied to asphalt elastic cured track bed, Constr. Build. Mater. 415 (2024), https://doi.org/10.1016/j.conbuildmat.2024.134921.

[24] T. Wang, C. Shi, Y. Yu, G. Xu, S. Liu, H. Wang, J. Yang, M. Gong, Y. Xu, L. Qie, Mechanical properties evaluation of crumb rubber asphalt mixture for elastic trackbed, Constr. Build. Mater. 331 (2022), https://doi.org/10.1016/j.conbuildmat.2022.127048.

[25] C. Shi, Y. Wu, C. Fu, J. Yang, Mechanical properties of rubberized epoxy asphalt mixture used in railway infrastructure. Advances in Functional Pavements, CRC Press, 2024, pp. 22–26, https://doi.org/10.1201/9781003387374-5.

[26] Y. Wu, P. Huang, Y. Yu, C. Shi, H. Chen, H. Wang, J. Yang, Z. Leng, W. Huang, Nonlinear rheological performance characterization of styrene-butadiene-styrene and crumb rubber composite modified bitumen using large amplitude oscillatory shear tests, J. Clean. Prod. 385 (2023) 135712, https://doi.org/10.1016/j.jclepro.2022.135712.

[27] C. Shi, Y. Wu, T. Wang, Y. Yu, H. Wang, J. Yang, Rheological properties and polymer phase structure characterization of SBS/CR composite modified asphalt (CMA) binders, Mater. Struct. 56 (2) (2023) 33, https://doi.org/10.1617/s11527-023-02122-y.

[28] H. Wang, V. Markine, Dynamic behaviour of the track in transitions zones considering the differential settlement, J. Sound. Vib. 459 (2019) 114863, https://doi.org/10.1016/j.jsv.2019.114863.

[29] H. Wang, V.L. Markine, Methodology for the comprehensive analysis of railway transition zones, Comput. Geotech. 99 (2018) 64–79, https://doi.org/10.1016/j.compgeo.2018.03.001.

[30] G. Jing, M. Siahkouhi, H. Wang, M. Esmaeili, The improvement of the dynamic behavior of railway bridge transition zone using furnace slag reinforcement: a numerical and experimental study, Proc. Inst. Mech. Eng. F-J. Rail Rapid Transit (2021) 09544097211020603, https://doi.org/10.1177/09544097211020603.

[31] J.Y. Shih, D. Thompson, A. Zervos, The effect of boundary conditions, model size and damping models in the finite element modelling of a moving load on a track/ground system, Soil Dyn. Earthq. Eng. 89 (2016) 12–27, https://doi.org/10.1016/j.soildyn.2016.07.004.

[32] Z. Yang, A. Boogaard, Z. Wei, J. Liu, R. Dollevoet, Z. Li, Numerical study of wheel-rail impact contact solutions at an insulated rail joint, Int. J. Mech. Sci. 138-139 (2018) 310–322, https://doi.org/10.1016/j.ijmecsci.2018.02.025.

[33] J.W. Nam, J.H.J. Kim, S.B. Kim, N.H. Yi, K.J. Byun, A study on mesh size dependency of finite element blast structural analysis induced by non-uniform pressure distribution from high explosive blast wave, KSCE J. Civ. Eng. 12 (4) (2008) 259–265, https://doi.org/10.1007/s12205-008-0259-x.

[34] H. Jiang, X. Bian, C. Cheng, Y. Chen, R. Chen, Simulating train moving loads in physical model testing of railway infrastructure and its numerical calibration, Acta Geotech. 11 (2) (2016) 231–242, https://doi.org/10.1007/s11440-014-0327-y.

[35] B. Liang, H. Luo, C.X. Sun, Simulated study on vibration load of high speed railway, 1) MOE key laboratory of high-speed railway engineering, Southwest Jiaotong University, Chengdu; 610031, China (2) China railway siyuan survey and design group Co., Ltd, Wuhan; 430063, China (3) Institute of architec Vol. 28(No. 4) (2006) 89–94.

[36] C. Shen, P. Zhang, R. Dollevoet, A. Zoeteman, Z. Li, Evaluating railway track stiffness using axle box accelerations: a digital twin approach, Mech. Syst. Signal. Process. 204 (2023), https://doi.org/10.1016/j.ymssp.2023.110730.

[37] C. Shen, X. Deng, Z. Wei, R. Dollevoet, A. Zoeteman, Z. Li, Comparisons between beam and continuum models for modelling wheel-rail impact at a singular rail surface defect, Int. J. Mech. Sci. 198 (2021), https://doi.org/10.1016/j.ijmecsci.2021.106400.

[38] H. Chen, A.R. Trivedi, C.R. Siviour, Application of linear viscoelastic continuum damage theory to the low and high strain rate response of thermoplastic polyurethane, Exp. Mech. 60 (7) (2020) 925–936, https://doi.org/10.1007/s11340-020-00608-2.

[39] C. Shi, Y. Wu, R. Fuentes, Y. Fan, Y. Zhou, C. Fu, J. Yang, Volumetric mix-design modification and vibration attenuation analysis of rubberised epoxy asphalt track for railway, Road Mater. Pavement Des. (2024) 1–24, https://doi.org/10.1080/14680629.2024.2432569.

[40] J.L. Humar, Dynamics of Structures, 3rd ed., CRC Press - Taylor & Francis Croup, 2012.

[41] A. Karlström, A. Boström, An analytical model for train-induced ground vibrations from railways, J. Sound. Vib. 292 (1–2) (2006) 221–241, https://doi.org/10.1016/j.jsv.2005.07.041.

[42] W. Zhai, Z. He, X. Song, Prediction of high-speed train induced ground vibration based on train-track-ground system model, Earthq. Eng. Eng. Vib. 9 (4) (2011) 545–554, https://doi.org/10.1007/s11803-010-0036-y.

[43] Y. Liu, Y. Fan, Y. Zhou, B. Chen, T. Hu, H. Wang, J. Yang, W. Huang, Analysis of low temperature performance and viscoelastic properties of SBS-modified epoxy recycled asphalt, Int. J. Pavement Eng. 26 (1) (2025), https://doi.org/10.1080/10298436.2025.2518150.

[44] A. Zofka, M. Maliszewski, A. Bernier, R. Josen, A. Vaitkus, R. Kleizienė, Advanced shear tester for evaluation of asphalt concrete under constant normal stiffness conditions, Road Mater. Pavement Des. 16 (sup1) (2015) 187–210, https://doi.org/10.1080/14680629.2015.1029690.

[45] Specifications for Design of Highway Asphalt Pavement, Ministry of Transport of the People's Republic of China, 2017.

[46] X. Xiao, J. Li, C. Wang, D. Cai, L. Lou, Y. Shi, F. Xiao, Numerical and experimental investigation of reduced temperature effect on asphalt concrete waterproofing layer in high-speed railway, Int. J. Rail Transp. 11 (3) (2022) 389–405, https://doi.org/10.1080/23248378.2022.2081879.

[47] Technical regulations for dynamic acceptance for high-speed railways construction, Ministry of Railways, China, 2013.

[48] Z. Friedman, J.B. Kosmatka, An improved two-node timoshenko beam finite element, Comput. Struct. 47 (3) (1993) 473–481, https://doi.org/10.1016/0045-7949(93)90243-7.